

Cold H I in faint dwarf galaxies

Narendra Nath Patra¹*, Jayaram N. Chengalur¹, Igor D. Karachentsev², Serafim S. Kaisin², Ayesha Begum³

¹ NCRA-TIFR, Post Bag 3, Ganeshkhind, Pune 411 007, India

² Special Astrophysical Observatory, Nizhniy Arkhyz, Karachai-Cherkessia 369167, Russia

³ IISER-Bhopal, ITI Campus (Gas Rahat) Building, Govindpura, Bhopal - 23, India.

ABSTRACT

We present the results of a study of the amount and distribution of cold atomic gas, as well as its correlation with recent star formation in a sample of extremely faint dwarf irregular galaxies. Our sample is drawn from the Faint Irregular Galaxy GMRT Survey (FIGGS) and its extension, FIGGS2. We use two different methods to identify cold atomic gas. In the first method, line-of-sight H I spectra were decomposed into multiple Gaussian components and narrow Gaussian components were identified as cold H I. In the second method, the brightness temperature (T_B) is used as a tracer of cold H I. We find that the amount of cold gas identified using the T_B method is significantly larger than the amount of gas identified using Gaussian decomposition. We also find that a large fraction of the cold gas identified using the T_B method is spatially coincident with regions of recent star formation, although the converse is not true. That is only a small fraction of the regions with recent star formation are also covered by cold gas. For regions where the star formation and the cold gas overlap, we study the relationship between the star formation rate density and the cold H I column density. We find that the star formation rate density has a power law dependence on the H I column density, but that the slope of this power law is significantly flatter than that of the canonical Kennicutt-Schmidt relation.

Key words: galaxies: dwarf - galaxies: evolution - galaxies: ISM

1 INTRODUCTION

The ISM in galaxies is multi-phase, consisting of molecular, atomic and ionised phases. Early observations of the H I 21cm emission/absorption spectra in our galaxy showed that the atomic gas itself has multiple phases (Clark 1965; Radhakrishnan & Goss 1972), a clumpy dense phase with low spin temperature and a more diffuse widely distributed phase with a high spin temperature. Theoretically it has been established that in steady state (i.e. when the heating rate is balanced by the cooling rate) the gas settles into one of two stable phases, a cold dense phase (the “Cold Neutral Medium” or CNM) and a warm diffuse phase (the “Warm Neutral Medium” or WNM) (Field & Saslaw 1965; Field, Goldsmith & Habing 1969; Wolfire et al. 1995a, 2003). In these models, gas at temperatures intermediate between that of the stable CNM and WNM is subject to thermal instability and is expected to settle into one of the two stable phases.

Gas in the CNM has small velocity dispersion and large 21cm optical depths, and is easily detected in absorption. The properties of the CNM in our galaxy are hence quite well established by emission/absorption studies. On the other hand the WNM has a very low optical depth, large velocity dispersion, is extremely challenging to

detect in absorption, and its properties hence remain observationally not very established. Theoretical studies however indicate that the timescales for gas that has been disturbed away from the stable WNM conditions to settle into the WNM can be quite large. Sensitive emission absorption studies done over the last decade, aimed partly at detecting the WNM in absorption (e.g. Heiles & Troland 2003a,c; Kanekar et al. 2003; Roy et al. 2013; Roy, Kanekar & Chengalur 2013a) have resulted in the somewhat surprising conclusion that a reasonable fraction of the atomic ISM in our galaxy could be out of thermal equilibrium, i.e. have temperatures that are intermediate between that of the CNM and WNM. Similarly numerical simulations of gas in a turbulent medium (e.g. Audit & Hennebelle 2005) have also shown that in steady state a reasonable fraction of the gas could have temperatures in the unstable range.

In the case of nearby dwarf galaxies, most earlier studies of the phase structure of the gas have been done in the context of the classical two phase models and have focused on using the velocity dispersion to distinguish between the CNM and WNM. Young & Lo (1997); Young et al. (2003); Begum, Chengalur & Bhardwaj (2006); Warren et al. (2012) all analysed the spatially resolved line-of-sight H I emission spectra of a number of nearby dwarf galaxies to look for narrow velocity dispersion gas. The narrow velocity dispersion gas was identified via multi-Gaussian fitting to the observed spectra. Components with small velocity dispersion were identified

* E-mail: narendra@ncra.tifr.res.in

as arising from the CNM, whereas components with large velocity dispersion were identified with the WNM.

In our own galaxy, it has observationally been established that large optical depths (implying presence of the CNM) can be found along all lines of sight where the HI 21cm brightness temperature exceeds some threshold value (Braun & Walterbos 1992; Roy et al. 2013). This can be understood in terms of a maximum brightness temperature that the WNM can produce. As discussed in more detail below, because of its low optical depth, there is a limit on how large a brightness temperature one can get from physically reasonably sized path lengths through the WNM. The presence of high brightness temperature gas can hence be used to locate dense cold gas in external galaxies (e.g. Braun 1997). Since the CNM is clumpy, this requires sensitive high spectral and velocity resolution observations. In this paper we use these two different methods to detect cold HI in our sample of galaxies and try to see its correlation with star formation.

2 SAMPLE & DATA REDUCTION

The sample of galaxies we use is drawn from the Faint Irregular Galaxy GMRT Survey (FIGGS) (Begum et al. 2008), and FIGGS2 survey (Patra et al. 2015 (submitted)). These two samples contain a total of 73 galaxies with HI interferometric images. As described in more detail below, for detecting CNM the galaxies needed to be imaged at a specific linear resolution. Out of the original sample of 73 galaxies, 11 galaxies could not be imaged at the required resolution, mainly because of signal to noise ratio related issues. The final sample hence consists of 62 galaxies. The median HI mass and median blue magnitude (M_B) of the sample are $10^{7.3} M_\odot$ and -12.7 respectively. Some general properties of the sample galaxies are listed in Tab. 1. The columns of the table are: col(1): Name of the galaxy, col(2): Other major surveys as part of which the galaxy was observed in HI, col(3): Right Ascension (J2000), col(4): Declination (J2000), col(5): the distance to the galaxy in Mpc (taken from (Karachentsev, Makarov & Kaisina 2013)) col(6): the method by which the distance is estimated, col(7): The absolute blue magnitude (M_B) (again taken from (Karachentsev, Makarov & Kaisina 2013)) col(8): The log of HI mass of the galaxy, col(9): Optical inclination of the galaxy, column(10) indicates if the galaxy is included in the sample used for detecting the CNM via the Gaussian Decomposition method (see Sec.3), column(11) indicates if the galaxy is included in the sample for detecting the CNM via the Brightness Temperature (T_B) method (see Sec.4), col(12) the velocity resolution used to image the galaxy at ~ 100 pc (as required for the T_B method).

As discussed above we use two different methods to try and identify gas in the CNM phase, viz. the Gaussian Decomposition method and Brightness Temperature (T_B) method. As shown in Sec. 3, the Gaussian Decomposition method requires spectra with high signal to noise ratio. For this we use data cubes at a uniform linear resolution of ~ 400 pc. Data cubes at higher linear resolutions have a signal to noise ratio that is too low for the Gaussian decomposition method to work reliably. On the other hand, as discussed in Sec. 4, the brightness temperature method is well suited to high resolution data cubes, and does not require as high signal to noise ratio spectra. We hence use data cubes made at ~ 100 pc linear resolution for finding cold gas using the brightness temperature method. Some galaxies from the parent sample did not have sufficient signal to noise ratio (SNR) in the low resolution ~ 400 pc data cubes, while some galaxies did not have sufficient snr in the

~ 100 pc data cubes. These galaxies were hence dropped from the sub-sample used for that particular method. Details of the actual galaxies that were used for each method are also given in Tab. 1.

3 SEARCHING FOR THE CNM USING GAUSSIAN DECOMPOSITION

Classical models for the phase structure of the atomic ISM in the Milkyway and nearby galaxies indicate the existence of two stable phases with kinetic temperatures $\sim 5000 - 8000$ K, i.e. the “Warm Neutral Medium” (WNM) and $\sim 50 - 300$ K, i.e. the “Cold Neutral Medium” (CNM) respectively (Wolfire et al. 1995b). Recent observations and models suggest that in addition, there could be a significant amount of gas with kinetic temperatures that lie between $500 - 5000$ K, i.e. in the range that is thermally unstable (see e.g. Heiles & Troland 2003b; Kanekar & Chengalur 2003; Roy, Kanekar & Chengalur 2013b; Kim, Ostriker & Kim 2014). We follow Chengalur, Kanekar & Roy (2013) in calling this as the “Unstable Neutral Medium” (UNM).

In the Gaussian decomposition method, one decomposes the line of sight velocity profile into multiple Gaussians, and identifies components with velocity widths corresponding to kinetic temperatures in the CNM range as the cold neutral medium. Gas at a temperature of 200 K would have a one dimensional thermal velocity dispersion of $\sim 1.28 \text{ km s}^{-1}$ or a FWHM of $\sim 3.1 \text{ km s}^{-1}$. However, most previous studies of the CNM in dwarf galaxies (see e.g. Young & Lo 1997; de Blok & Walter 2006; Warren et al. 2012) have used significantly larger velocity dispersions (up to $\sim 6 \text{ km s}^{-1}$) to identify CNM gas. We note that a velocity dispersion of $\sim 6 \text{ km s}^{-1}$ corresponds to kinetic temperatures of ~ 4400 K. While this temperature is significantly higher than the maximum expected for the CNM, it is nonetheless lower than the expected kinetic temperature for the WNM. In the absence of non thermal contributions to the velocity width, gas with velocity dispersion $\lesssim 6 \text{ km s}^{-1}$ would correspond to gas in phases other than the WNM, i.e. the CNM or UNM.

In the presence of non-thermal motions however, the situation is more complex (see Roy et al. (2013) for a detailed discussion). The simplest case is if one assumes that the gas is iso-thermal and that the only non-thermal motions are micro-turbulence and that the net effect of these motions is to keep the profile shape as a Gaussian, albeit with a larger velocity width than that corresponding to the kinetic temperature. In this case, the velocity width of the profile provides an upper limit to the kinetic temperature, and gas with velocity dispersion of $\sim 6 \text{ km s}^{-1}$ must be at a kinetic temperature lower than that corresponding to the WNM. However if the gas has a range of temperatures, or if because of bulk motions the line profile is intrinsically non-Gaussian, then it is not clear what the components derived from a Gaussian decomposition physically correspond to. In this section, we follow earlier studies (i.e. those cited above, as well as galactic studies such as Shuter & Verschuur (1964); Heiles & Troland (2003b)) in assuming that the velocity width obtained from Gaussian decomposition can be used as a proxy for the kinetic temperature, but we return to the issues raised above in Sec. 4.

3.1 Implementation

Line-of-sight HI spectra were extracted from the 400 pc image cubes and decomposed into multiple Gaussian components using a python routine ‘multigauss’ that was developed by us for this

Table 1. General properties of our sample galaxies.

Name	Other surveys*	RA (J2000)	DEC (J2000)	Dist (Mpc)	Method	M _B (mag)	log M_{HI} (M _⊙)	i _{opt} (°)	Gaussian	T _B	Δv (T _B) (km s ⁻¹)
DDO226	—	004303.8	-221501	4.92	TRGB	-13.6	7.53	90	Y	N	—
DDO006	2	004949.3	-210058	3.34	TRGB	-12.4	7.04	90	N	N	3.3
UGC00685	—	010722.3	+164102	4.51	TRGB	-14.3	7.74	51	Y	Y	6.6
KKH6	—	013451.6	+520530	3.73	TRGB	-12.4	6.63	62	Y	Y	3.3
AGC112521	3	014107.9	+271926	6.58	TRGB	-11.6	6.82	67	N	N	—
KK14	3	014442.7	+271716	7.20	mem	-12.1	7.56	90	N	N	—
KK15	3	014641.6	+264805	9.04	TRGB	-11.9	7.24	90	N	N	—
KKH11	—	022435.0	+560042	3.00	mem	-13.3	7.66	68	Y	Y	1.7
KKH12	—	022727.0	+572916	3.00	mem	-13.0	7.23	90	N	N	1.6
KKH34	—	055941.2	+732539	4.61	TRGB	-12.3	6.76	66	N	Y	3.3
ESO490-017	—	063756.6	-255959	4.23	TRGB	-14.5	7.55	46	N	N	—
KKH37	2	064745.8	+800726	3.39	TRGB	-11.6	6.70	55	N	N	—
UGC03755	—	071351.8	+103119	7.41	TRGB	-15.7	8.25	63	N	N	—
DDO043	1	072817.2	+404613	5.73	BS	-13.9	7.85	53	N	N	—
KK65	—	074231.2	+163340	8.02	TRGB	-14.3	7.70	66	N	N	—
UGC04115	—	075701.8	+142327	7.73	TRGB	-14.3	8.34	66	Y	N	—
KK69	—	085250.7	+334752	7.70	mem	-12.2	7.51	46	N	N	—
KKH46	—	090836.6	+051732	5.60	h	-11.9	7.28	34	N	N	—
UGC04879	—	091602.2	+525024	1.36	TRGB	-11.9	5.98	66	N	N	—
UGC05186	—	094259.8	+331552	8.30	TF	-13.4	7.38	90	N	N	—
UGC05209	—	094504.2	+321418	6.56	h	-13.1	7.15	18	N	Y	3.3
UGC05456	—	100719.7	+102144	5.60	TRGB	-15.1	7.71	72	Y	N	—
LeG06	—	103955.7	+135428	10.40	mem	-11.9	6.85	57	N	N	—
KDG073	2	105257.1	+693245	3.70	TRGB	-10.8	6.51	38	N	N	—
UGC06145	—	110535.0	-015149	10.70	mem	-13.9	7.97	66	N	N	—
UGC06456	1	112800.6	+785929	4.35	TRGB	-14.1	7.77	69	N	Y	1.6
UGC06541	1	113329.1	+491417	3.89	TRGB	-13.6	6.97	65	N	Y	3.3
KK109	—	114711.2	+434019	4.51	TRGB	-10.3	6.54	55	N	N	—
DDO099	2	115053.0	+385250	2.64	TRGB	-13.5	7.74	90	N	N	3.3
ESO379-007	—	115443.0	-333329	5.22	TRGB	-12.3	7.51	49	Y	Y	1.7
ESO321-014	—	121349.6	-381353	3.18	TRGB	-12.7	7.21	83	N	N	—
UGC07298	—	121628.6	+521338	4.21	TRGB	-12.3	7.28	67	Y	Y	1.7
VCC0381	—	121954.1	+063957	4.71	h	-11.7	7.14	26	N	N	—
KK141	—	122252.7	+334943	7.78	h	-12.9	7.20	45	N	N	—
IC3308	—	122517.9	+264253	12.80	TF	-15.5	8.57	77	N	N	—
KK144	—	122527.9	+282857	6.15	h	-12.5	7.86	81	N	N	—
DDO125	2	122741.8	+432938	2.74	TRGB	-14.3	7.48	66	N	Y	1.7
UGC07605	—	122839.0	+354305	4.43	TRGB	-13.5	7.32	49	Y	Y	3.3
KK152	—	123324.9	+332105	6.90	TF	-13.0	7.54	83	N	N	—
UGCA292	1, 2	123840.0	+324600	3.61	TRGB	-11.8	7.44	52	N	Y	1.7
BTS146	—	124002.1	+380002	8.50	TF	-12.2	6.97	67	N	N	—
LVJ1243+4127	—	124355.7	+412725	6.09	h	-11.8	7.02	83	N	N	—
KK160	—	124357.4	+433941	4.31	TRGB	-10.9	6.59	47	N	N	—
UGC08055	—	125604.0	+034841	13.00	TRGB	-13.7	8.89	36	N	N	—
GR8	1, 2	125840.4	+141303	2.13	TRGB	-12.0	6.89	27	N	Y	1.7
UGC08215	—	130803.6	+464941	4.55	TRGB	-12.3	7.27	52	Y	Y	3.3
DDO167	1	131322.8	+461911	4.19	TRGB	-12.7	7.19	67	N	N	—
KK195	—	132108.2	-313147	5.22	TRGB	-11.8	7.56	78	N	N	—
KK200	—	132436.0	-305820	4.63	TRGB	-12.0	6.84	60	Y	Y	1.7
UGC08508	1, 2	133044.4	+545436	2.69	TRGB	-13.1	7.30	63	N	Y	1.7
UGCA365	—	133630.8	-291411	5.25	TRGB	-13.3	7.26	87	N	N	—
UGC08638	—	133919.4	+244633	4.27	TRGB	-13.7	7.08	55	Y	N	—
DDO181	2	133953.8	+404421	3.01	TRGB	-13.2	7.33	65	N	N	—
IC4316	—	134018.1	-285340	4.41	TRGB	-13.9	7.05	59	N	N	—
DDO183	2	135051.1	+380116	3.22	TRGB	-13.2	7.31	90	N	N	1.7
KKH86	2	135433.6	+041435	2.59	TRGB	-10.3	5.91	51	N	N	—
UGC08833	2	135448.7	+355015	3.08	TRGB	-12.2	7.00	30	N	Y	1.7
DDO187	1, 2	141556.5	+230319	2.20	TRGB	-12.4	7.06	46	N	Y	3.3
PGC051659	—	142803.7	-461806	3.58	TRGB	-13.1	7.78	90	N	N	1.7
KK246	—	200357.4	-314054	7.83	TRGB	-13.7	8.07	87	N	N	—
DDO210	1	204651.8	-125053	0.94	TRGB	-11.1	6.42	72	N	N	1.6
KKH98	2	234534.0	+384304	2.45	TRGB	-10.8	6.45	67	N	Y	3.3

* Survey notations , 1 = LITTLE-THINGS (Hunter et al. 2012) , 2 = VLA-ANGST (Ott et al. 2012) , 3 = SHIELD (Cannon et al. 2011)

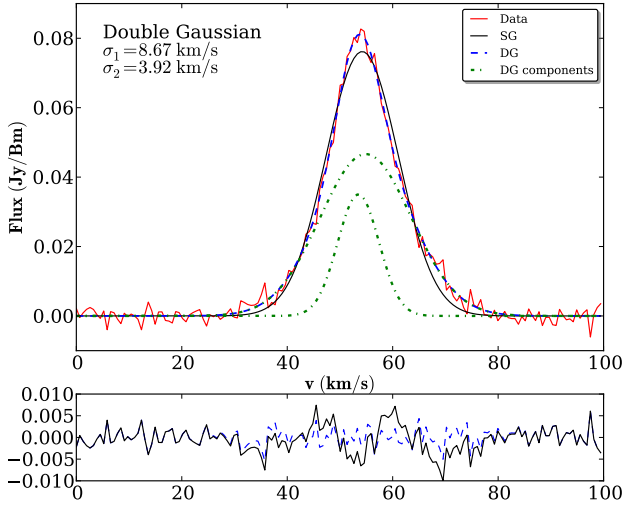


Figure 1. Example fits at SNR=20. The (simulated) input data (red solid noisy line), a single Gaussian fit (black solid smooth line), double Gaussian fit (blue dashed line) as well as the individual components of the double Gaussian fit (dotted lines) are shown. The residuals after subtracting the fits from the data are also shown (dashed line residual from the double Gaussian fit, solid line residual from the single Gaussian fit). The routine detects a double gaussian fit as the best fit. The velocity dispersions for the double Gaussian fit are $\sigma_1 = 8.67 \text{ km s}^{-1}$ and $\sigma_2 = 3.92 \text{ km s}^{-1}$, which match the true input values (8 km s^{-1} and 4 km s^{-1}) very well.

purpose. ‘multigauss’ uses a non-linear optimization routine as implemented using the ‘lmfit’ python package.

Starting with a single Gaussian component, Gaussian components were successively added to the model till there is no improvement in the fit residuals as interpreted by a single-tailed F-test. This is similar to the procedure followed earlier by Warren et al. (2012). A single-tailed F-test estimates the probability (or confidence level) that two fit residuals are different just by random chance. Two residuals, one with N components and another with $N+1$ components are compared by single-tailed F test and the question asked is: what is the confidence level with which one can reject the hypothesis that the residual of fit with $N+1$ components is better than the residual of fit with N components purely by chance. This confidence level is referred as F-test confidence level of rejecting the null hypothesis.

Narrow components returned by the routine were accepted as representing cold gas if the following criteria are met. (1) The component must have a velocity dispersion $\sigma \lesssim 6 \text{ km s}^{-1}$, (2) the amplitude of the narrow component must be at least 3 times the per channel rms noise, and (3) the velocity dispersion of the component must be greater than the velocity resolution of the data by at least the standard error returned by the fitting routine. Conditions (2) and (3) are meant to reduce the possibility of falsely identifying a narrow noise spike as a genuine narrow component. There was no restriction placed on the central velocity of the components. These criteria are very similar to those used in past studies, e.g. (Young & Lo 1997; de Blok & Walter 2006; Warren et al. 2012). One important difference between the current routine and those used in previous studies is that previous studies limited the maximum number of Gaussian components per spectrum to 2, whereas in the current decomposition the total number of components to be fit has been

Table 2. Characterization of the efficiency and the accuracy of the decomposition routine

Confidence level	$A_{\text{sim}}/A_{\text{extr}}$	$\Delta b \text{ (km/s)}$	$\Delta \sigma \text{ (km/s)}$
95%	0.97 ± 0.17	0.00 ± 0.26	-0.12 ± 0.57
90%	0.98 ± 0.21	0.00 ± 0.35	-0.07 ± 0.57
80%	0.99 ± 0.29	-0.01 ± 0.58	0.00 ± 0.60
70%	1.02 ± 0.36	0.00 ± 0.74	-0.06 ± 0.69

left as a free parameter. All of our spectra are however well described by single or double Gaussian, with no spectra having more than two components in the best fit model.

In Fig. 1 we show an example of the decomposition done by the ‘multigauss’ routine. The input simulated spectrum has an SNR = 20 with two Gaussian components of width 4 km s^{-1} and 8 km s^{-1} . From Fig. 1 one can see that the routine correctly finds a double Gaussian fit better describes the spectra than a single Gaussian fit. Our routine also correctly recovers the velocity widths of two different input components. See Figure caption for more details.

3.1.1 Characterization of the routine

To characterize the detection efficiency of our routine multigauss, 50,000 model spectra were simulated having global SNR distributed uniformly between $10 < \text{SNR} < 60$. Each spectrum consisted of a narrow component with $\Delta v < \sigma < 6.0 \text{ km s}^{-1}$, (where Δv is set 1.65 km s^{-1} , i.e. corresponding to the velocity resolution of the observed data) and a broad component with $8.0 < \sigma < 12.0 \text{ km s}^{-1}$. Each of the components was required to have a SNR (i.e. peak amplitude) more than 3. Adopting a conservative approach, the centroids of two components were set to be the same, as any offset between these two would lead to a higher detection efficiency. As mentioned above, no spectra required more than two components for the best fit; the simulated spectra were hence restricted not to have more than two components. These synthetic spectra then passed through the multigauss routine. In Figure 2 (left panel), we plot the recovery efficiency of our routine as a function of SNR. Different curves represent different confidence levels of F-test.

To characterize the false detection rate of our routine, we simulated 1000 spectra with only one component with velocity dispersion uniformly distributed between $8.0 < \sigma < 12.0 \text{ km s}^{-1}$, added gaussian random noise, and then passed them through multigauss. The false positive detection rate measured in this way is shown in Fig.2 (right panel). We note that the false positive rate is always less than a few percent for our working range of SNR (i.e. > 10). This is similar to the results found in previous studies (e.g. Warren et al. 2012). The detection efficiency and detection accuracy are summarized in Table 2. The columns in the table are as follows: Col. (1) the confidence level of the F-test. Col. (2) the amplitude ratio of the input and recovered narrow component. Col. (3) the mean offset between the centroids of the input and recovered narrow component. Col. (4) The average of the absolute value of the difference between input and the recovered velocity dispersion of the narrow component. We note that the offset in the recovered quantities are in all cases small compared to the scatter between runs. As such there are no significant trends in the recovered quantities.

For the rest of the analysis below we adopt a conservative F-

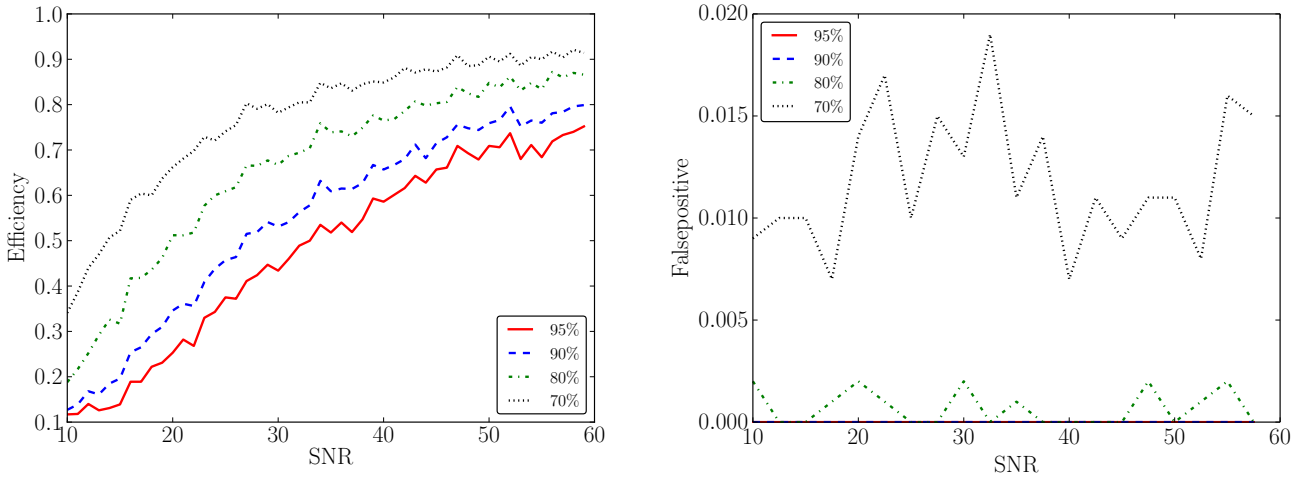


Figure 2. The recovery efficiency of our routine as a function of the signal to noise ratio (SNR) at different F-test confidence levels. Right panel: False detection rate of our routine as a function of the SNR at different F-test confidence limits.

test confidence level, which we set to 95%. At this confidence level, the detection rate is comparatively small, but the false positive rate is negligible. Further, in the cases where a narrow component is recovered, the parameters of this Gaussian are also fairly accurately recovered. Using this conservative approach implies that the number of identified narrow components is a lower limit to the true number of such components. Once again the approach adopted here is similar to that taken in earlier studies (e.g. Warren et al. 2012), to allow an easy comparison of our results with those from earlier work.

To compare our routine with previous work we show in Fig. 3 the regions with narrow velocity components in the galaxy DDO183 as identified using the ‘multigauss’ routine (left panel) as well as the regions identified by Warren et al. (2012) (right panel). The black contours in both the panels show the H I column density at 10^{20} and 10^{21} atoms cm^{-2} . The red contours (left panel) and red region (right panel) marks the locations of detected narrow velocity dispersion H I. Fig. 3 shows that our routine compares reasonably well with previous work. Narrow velocity dispersion H I is identified at similar locations in spite of the data being taken with two different telescopes (GMRT and JVLA respectively) at two different spatial resolutions (400 kpc and 200 kpc respectively).

We also passed some of the publicly available data from LITTLE-THINGS (Hunter et al. 2012) survey through the ‘multigauss’ routine. The narrow velocity dispersion detected by ‘multigauss’ matches well with the published results by (Warren et al. 2012).

3.2 Results

Our parent sample consist of 62 galaxies. For galaxies with high inclinations, the observed spectrum is a blend of the emission from gas distributed along a relatively long line of sight. We hence exclude galaxies with inclination more than 70° from the sample. As discussed above we also require a peak SNR of > 10 , and galaxies for which the data cube contained no spectra with SNR greater than this threshold were also dropped from the sample. After these cuts, we are left with a total of 13 galaxies.

The data for these 13 galaxies were passed through the *multigauss* routine, which detected narrow components in 5 of them. In Table 3 we summarise the inputs and the results of Gaussian decomposition method. The columns are as follows: Col. (1) Name of the galaxy, Col. (2) The log of H I mass of the galaxy, Col. (3) The absolute blue magnitude of the galaxy, Col. (4) The number of lines-of-sight which met the SNR criteria (i.e. $\text{SNR} > 10$), Col. (5) Column density at $\text{SNR} = 10$, Col. (6) the average SNR of the spectra with SNR greater than the threshold, Col. (7) shows the average column density of the lines-of-sight having SNR greater than 10. Col. (8) The peak column density in the galaxy, and Col. (9) The amount of narrow velocity dispersion H I detected.

Figure 4 shows the narrow velocity dispersion H I detected in the galaxy UGC 685. The dashed line contours show the integrated H I emission, while the $\text{H}\alpha$ emission is shown in grey-scales. The regions where narrow velocity dispersion H I were detected is delineated by solid lines.

We note that the narrow velocity dispersion H I as detected by the Gaussian decomposition method doesn’t coincide with the highest column density regions or with the $\text{H}\alpha$ emission. The $\text{H}\alpha$ emission originates mainly from regions with recent (i.e. 3 – 10 Myr) star-formation. For all of our sample galaxies, the narrow velocity dispersion H I is offset from the regions of current star formation. If the CNM is associated with the gas in which the star formation occurs, one would expect that there would be a good correlation between the detected CNM and the $\text{H}\alpha$ emission. We note that previous studies (Young & Lo 1996; Warren et al. 2012) also observed similar offset between the gas with small velocity dispersion and the regions of current star formation. One possible explanation is that in this context, the Gaussian Decomposition method is not best suited for identifying the CNM in dwarf galaxies. We explore this possibility, as well as other techniques to identify the CNM in the rest of this paper.

3.3 Drawbacks of Gaussian decomposition method

As described above we used (following earlier studies of the CNM in nearby dwarf galaxies) Gaussian decomposition to identify narrow velocity dispersion gas. This method has several drawbacks.

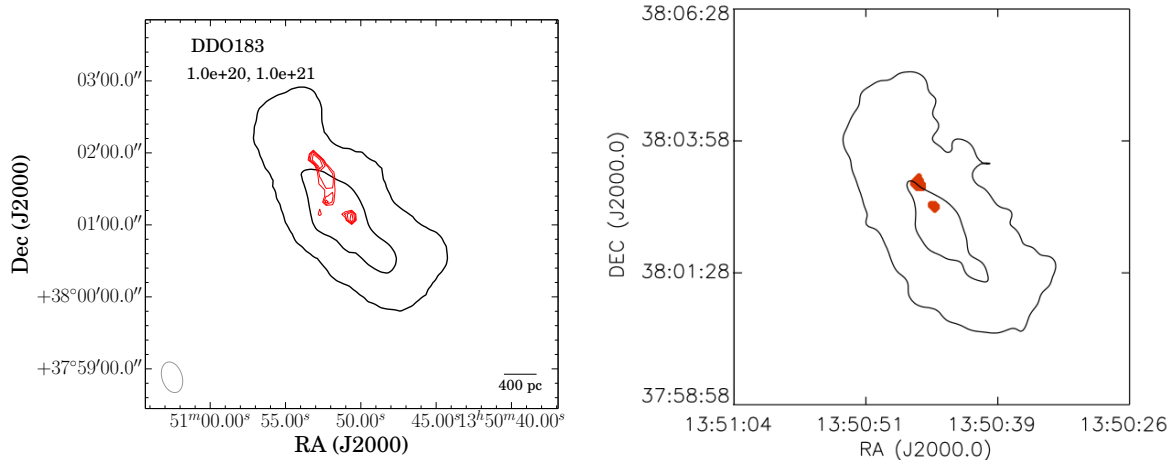


Figure 3. Left panel: Recovered cold HI in DDO183 using ‘multigauss’ routine. Right panel: Recovered cold HI using Gaussian decomposition method by Warren et al. (2012)

Table 3. Summary of cold HI search using Gaussian decomposition method

Name	$\log M_{\text{HI}}$ (M_{\odot})	M_B	N	CD_{10} ($\times 10^{19} \text{ cm}^{-2}$)	$\langle \text{SNR} \rangle$	$\langle CD \rangle$ ($\times 10^{19} \text{ cm}^{-2}$)	CD_{peak} ($\times 10^{19} \text{ cm}^{-2}$)	Cold M_{HI} ($\times 10^5 M_{\odot}$)	Δ Cold M_{HI} ($\times 10^5 M_{\odot}$)
DDO226	7.53	-13.6	2	10.70	10.07	10.80	10.80	—	—
UGC00685	7.74	-14.3	220	15.30	11.81	17.20	22.30	8.72	2.46
KKH6	6.63	-12.4	19	9.63	10.81	10.40	11.10	—	—
KKH11	7.66	-13.3	716	6.01	12.65	7.22	11.50	6.11	3.72
UGC04115	8.34	-14.3	8	18.70	10.18	19.00	19.50	—	—
UGC05456	7.71	-15.1	27	12.90	10.58	13.70	14.50	—	—
ESO379-007	7.51	-12.3	11	10.90	10.74	11.60	12.30	—	—
UGC07298	7.28	-12.3	1	10.40	10.01	10.40	10.40	—	—
UGC07605	7.32	-13.5	105	11.80	12.03	13.60	18.10	0.17	0.04
UGC08215	7.27	-12.3	13	14.00	10.56	14.70	15.60	1.91	0.98
KK200	6.84	-12.0	3	14.20	10.37	14.70	15.00	0.11	0.06
UGC08638	7.08	-13.7	16	13.40	10.30	13.80	14.20	—	—

The first is that, as is well known, Gaussians do not form an orthogonal basis set. Thus any Gaussian decomposition suffers from the problem of not being unique. Further as mentioned above, it is not clear that the components recovered from a given decomposition correspond to separate physical entities. Finally the shapes of the line profiles obtained using observations with finite spatial resolution (as well as integration along the line of sight) are determined by a number of physical processes, including turbulent motions and bulk velocities in addition to the thermal velocity dispersion. In view of these drawbacks, we examine in the next section, an alternate method for identifying cold atomic gas in dwarf galaxies.

4 THE BRIGHTNESS TEMPERATURE METHOD

The observed brightness temperature of HI 21cm emission (defined as $T_B = \frac{I_{\nu} c^2}{2k\nu^2}$ where T_B is the brightness temperature in Kelvin, ‘ I_{ν} ’ is the specific intensity, ‘ k ’ is Planck’s constant and ‘ c ’ is the speed of light), has long been used to constrain the physical conditions in the atomic ISM (e.g. Schmidt 1957; Rohlfs 1971; Baker & Burton 1975; Braun & Walterbos 1992). In detail, the observed brightness temperature depends on the distribution of the spin temperature, optical depth as well as spatial ordering of all the gas

along the line of sight. In the context of multi-phase models however, the presence of high brightness temperature gas is generally indicative of the presence of a cold dense phase along the line of sight. This is because in these models the warm gas generally has too low an optical depth to contribute more than a few degrees Kelvin to the brightness temperature. Consistent with this, Galactic studies show that, there is no detectable HI absorption along lines of sight where the emission brightness temperature, $T_B < 3 - 10\text{K}$ and almost all line-of-sights with $T_B > 3 - 10\text{K}$ have detectable absorption (Braun & Walterbos 1992; Roy, Kanekar & Chengalur 2013b). Braun & Walterbos (1992) and Braun (1997) also show that the HI emission observations of gas in the Milkyway and M31 can be well fit with models in which the brightness temperature is correlated to the opacity. An alternative method for searching for the CNM would then be to look for gas with brightness temperature much larger than say $\sim 10\text{K}$. Indeed this method has previously been used to identify cold, optically thick gas in external galaxies by Braun & Walterbos (1992); Braun (1997, 2012). We refer to this the brightness temperature method (or T_B method) for detecting the CNM.

Since gas in the CNM phase is expected to be clumpy, a high resolution HI image is a primary requirement to identify the high density cold HI in the brightness temperature method. In low reso-

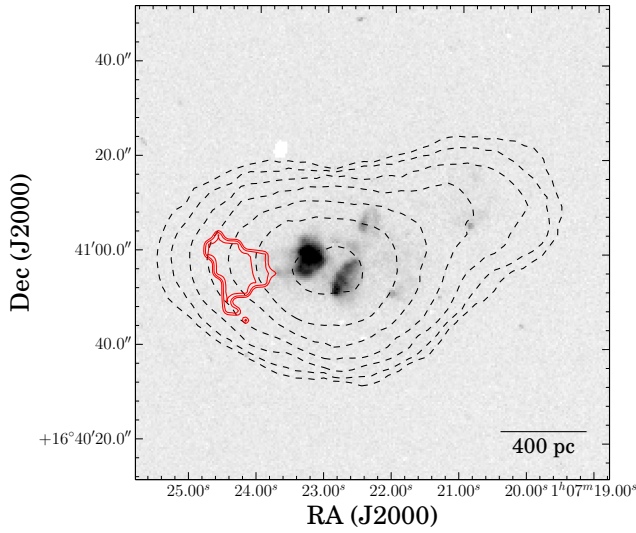


Figure 4. Gray scale represents the $H\alpha$ map of U685. Black broken contours represents total HI column density and the levels are (1, 1.4, 2, 2.8, 4, 5.6, 8, 11.2, 16, 22.4, ...) 5×10^{20} atoms cm^{-2} . Red solid contours show the cold HI as recovered by Gaussian method. The levels are (1, 1.4, 2, 2.8, 4, 5.6, 8, 11.2, 16, 22.4, ...) 6.2×10^{20} atoms cm^{-2} . The spatial resolution of the grey scale and the overlays are ~ 400 pc.

lution images the high T_B regions will be smoothed over, reducing ones ability to detect the compact peaks. The first step in trying this method on our sample galaxies was hence to re-image all of the galaxies at a spatial resolution of ~ 100 pc. Since for many galaxies the SNR is modest at this high resolution, the data were smoothed up to a velocity resolution of ~ 5 km s^{-1} wherever it was necessary (see Tab. 1). We note that the parameters that we use here (i.e. spatial resolution of ~ 100 pc and a velocity resolution of ~ 5 km s^{-1}) are similar to those used by (Braun 1997) to identify high brightness temperature gas.

We then inspected all of the data cubes to make sure that any emission that we detect is present at more than a 2σ level in several contiguous channels (of typically 1.6 km s^{-1} velocity width). We show for example in Fig. 5 the channel maps for UGC 685 at a spatial resolution of ~ 100 pc. The cross traces the location of one of the detected emission regions. As can be seen there is emission in velocities from 231 to 204 km s^{-1} .

In the two-phase models of the ISM (Wolfire et al. 1995b) at low metallicity and low dust content (as would be appropriate for our dwarf galaxies), the density of the WNM is expected to be in the range of $0.19 - 1.9$ atoms cm^{-3} and the spin temperature in the range of $5900 - 8400$ K (Wolfire et al. 1995a). For a region of size ~ 100 pc, the expected optical depth would then be $\lesssim 0.0031$, and the brightness temperature $\lesssim 18$ K. We hence conservatively set a threshold brightness temperature cutoff of $T_B > 50$ K to identify gas that arises from phases other than the classical WNM. For some galaxies, the per channel 2σ rms corresponded to T_B larger than 50 K, for these galaxies the 2σ level was instead used as a cut-off. The actual cut-off used per galaxy is listed in Tab. 4. Once we have identified gas with high brightness temperature (which we henceforth refer to as “cold” gas), the next step is to determine the total HI mass producing this emission. Two different approaches were adopted to calculate the cold HI mass from the emission brightness. In first case we assume that the emission is optically thin,

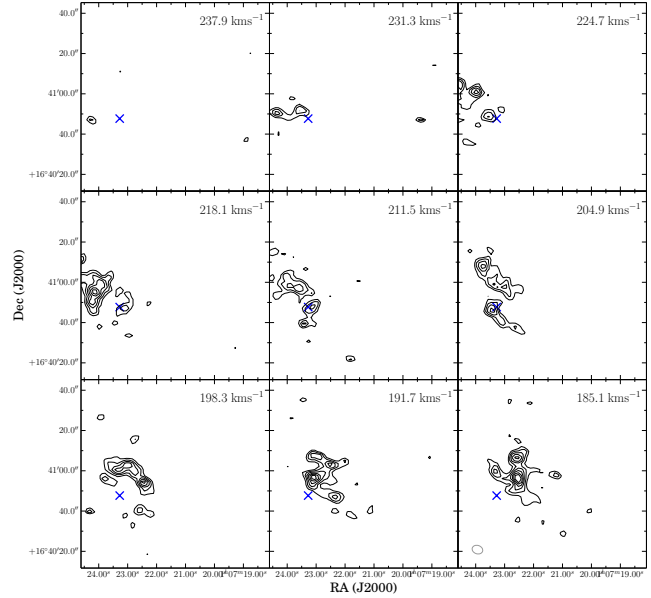


Figure 5. The HI channel maps of the galaxy UGC 685 at a spatial resolution of ~ 100 pc. The cross mark spots an emission region, which is seen over several contiguous channels (viz. a velocity range from 231 km s^{-1} to 204 km s^{-1}). Our moment map parameters were tuned to pick up only such clearly coherent structures.

in which case the total column density can be trivially computed from the moment map. This provides a lower limit to the cold HI mass. Our second approach was to assume that the emitting gas has a spin-temperature of 500 K, which is a robust upper limit in the two phase models (Wolfire et al. 1995b) for low metallicity gas. We calculated both estimates of the HI mass for all of galaxies in our sample.

4.1 Results

The GMRT has a hybrid configuration (Swarup et al. 1991), and for most of our observations the UV coverage allows one to make images at spatial resolutions as high as $\sim 4''$. For the analysis below we wish to use a uniform linear resolution, which we require to lie within the range $100 - 150$ pc. For 24 of the 62 galaxies in our sample either there was insufficient signal to noise ratio, or the galaxies were too distant for us to make images with $100 - 150$ pc resolution. These galaxies were dropped from the sample. A highly inclined galaxy would provide a much longer line-of-sight, leaving a possibility of producing high brightness temperature out of low density gas. To avoid these circumstances we further exclude another 10 galaxies from the sample which have inclination more than 70° . High resolution images were made for the remaining 28 galaxies, and high brightness temperature emission (i.e. “cold HI”) was detected in 19 of them, corresponding to a detection efficiency of $\sim 67\%$.

In Table 4 we summarise the results of the cold HI detected using the T_B method. The columns of the table are: Col. (1) the galaxy name. Col. (2) log of the HI mass (in solar units) Col. (3) the absolute blue magnitude Col. (4) the T_B cutoff used to identify cold HI. We set the cut off to 50K or 2σ , whichever is larger. Col. (5) the mass of cold HI estimated assuming the emission to be optically thin. Col. (6) error in the cold HI mass (optically thin)

Table 4. Summary of cold HI search using T_B method.

Name	$\log M_{\text{HI}}$ (M_\odot)	M_B	$(T_B)_{\text{cut}}$ (K)	$(M_{\text{HI}})_{\text{thin}}$ ($\times 10^5 M_\odot$)	$\Delta(M_{\text{HI}})_{\text{thin}}$ ($\times 10^5 M_\odot$)	$(M_{\text{HI}})_{500\text{K}}$ ($\times 10^5 M_\odot$)	$\Delta(M_{\text{HI}})_{500\text{K}}$ ($\times 10^5 M_\odot$)
UGC00685	7.74	-14.3	64	315.00	102.00	354.00	104.00
KKH6	6.63	-12.4	67	22.90	7.55	25.70	7.76
KKH11	7.66	-13.3	50	125.00	34.20	133.00	34.50
KKH34	6.76	-12.3	69	5.41	1.75	6.12	1.80
UGC05209	7.15	-13.1	55	14.80	5.01	16.20	5.11
UGC06456	7.77	-14.1	104	19.10	6.93	22.60	7.26
UGC06541	6.97	-13.6	58	31.40	10.30	34.70	10.60
ESO379-007	7.51	-12.3	51	78.70	26.20	85.60	26.60
UGC07298	7.28	-12.3	64	14.60	4.80	16.30	4.92
DDO125	7.48	-14.3	60	3.79	1.31	4.17	1.34
UGC07605	7.32	-13.5	53	63.60	19.40	70.30	19.80
UGCA292	7.44	-11.8	102	173.00	58.30	209.00	61.00
GR8	6.89	-12.0	50	4.64	0.77	4.90	0.77
UGC08215	7.27	-12.3	57	34.30	10.70	38.20	10.90
KK200	6.84	-12.0	53	23.10	7.45	25.30	7.59
UGC08508	7.30	-13.1	50	113.00	32.30	123.00	32.80
UGC08833	7.00	-12.2	50	40.40	10.70	43.50	10.90
DDO187	7.06	-12.4	139	24.80	8.34	33.40	8.91
KKH98	6.45	-10.8	50	4.76	1.25	5.07	1.27

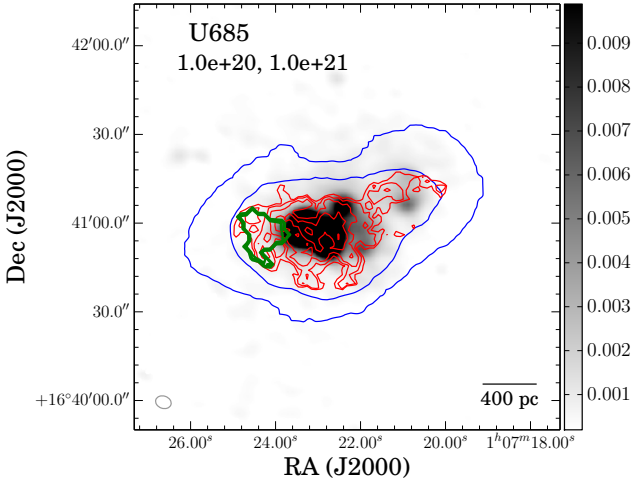


Figure 6. Cold HI as recovered by two different methods shown in contours overlaid on $H\alpha$ map in gray scale. The red solid contours represent cold HI recovered by T_B method and the green thick contours are the same for Gaussian decomposition method. The contours levels are (1, 1.4, 2, 2.8, 4, 5.6, 8, 11.2, 16, 22.4, ...) 1.5×10^{21} atoms cm^{-2} for cold HI detected by T_B method (red solid contours) and (1, 1.4, 2, 2.8, 4, 5.6, 8, 11.2, 16, 22.4, ...) 6.2×10^{20} atoms cm^{-2} for cold HI recovered by Gaussian decomposition method (green thick contours). The spatial resolution of $H\alpha$ data and the T_B data is ~ 100 pc.

Col. (7) the mass of cold HI estimated assuming the emission to be originated from a gas of spin temperature 500 K. Col. (8) error in the cold HI mass (assuming a 500 K spin temperature gas)

In Fig. 6 we show the cold HI as detected by the T_B method as well as the Gaussian decomposition method overlaid on the $H\alpha$ emission for UGC 685. The red solid contour represents the cold HI identified using the T_B method, whereas the green thick contours show the cold HI identified by the Gaussian decomposition method. From the plot one can see that the T_B method identifies gas that

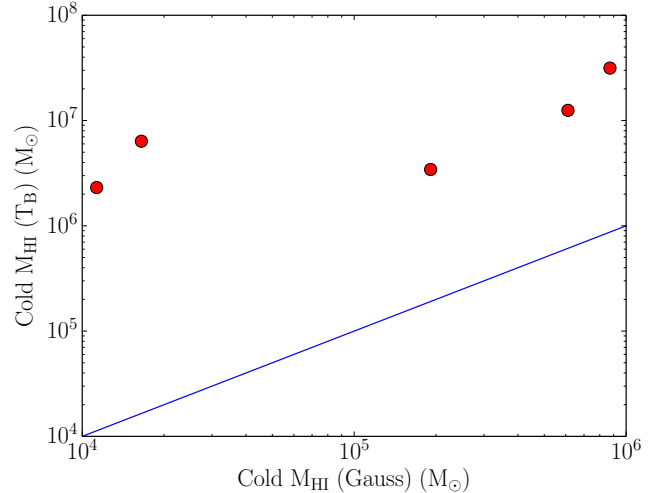


Figure 7. Comparison of cold HI mass estimated in the two different methods as discussed in the text. The blue solid line represent the 1:1 limit. From the figure it can be seen clearly that T_B method recovers more cold HI as compared to Gaussian decomposition method, however no obvious trend between the detected cold HI in T_B method and in Gaussian decomposition method can be found.

correlates with the $H\alpha$ emission better than the Gaussian decomposition method. For an easy comparison of our data and imaging quality as well as the locations of detected cold HI using different methods, we overplot $H\alpha$, cold HI (Gaussian and T_B method) with different star formation tracers ($H\alpha$ and FUV) in Appendix (Fig. 16 to Fig. 22). In Fig. 7 we compare the cold HI recovered by both the methods. As can be seen T_B method recovers significantly more ‘cold’ gas than the Gaussian decomposition method. In Fig. 8 we plot the histograms of detected cold gas fraction in both the methods. Once again it is clear that the T_B method identifies much more cold gas than the Gaussian Decomposition method.

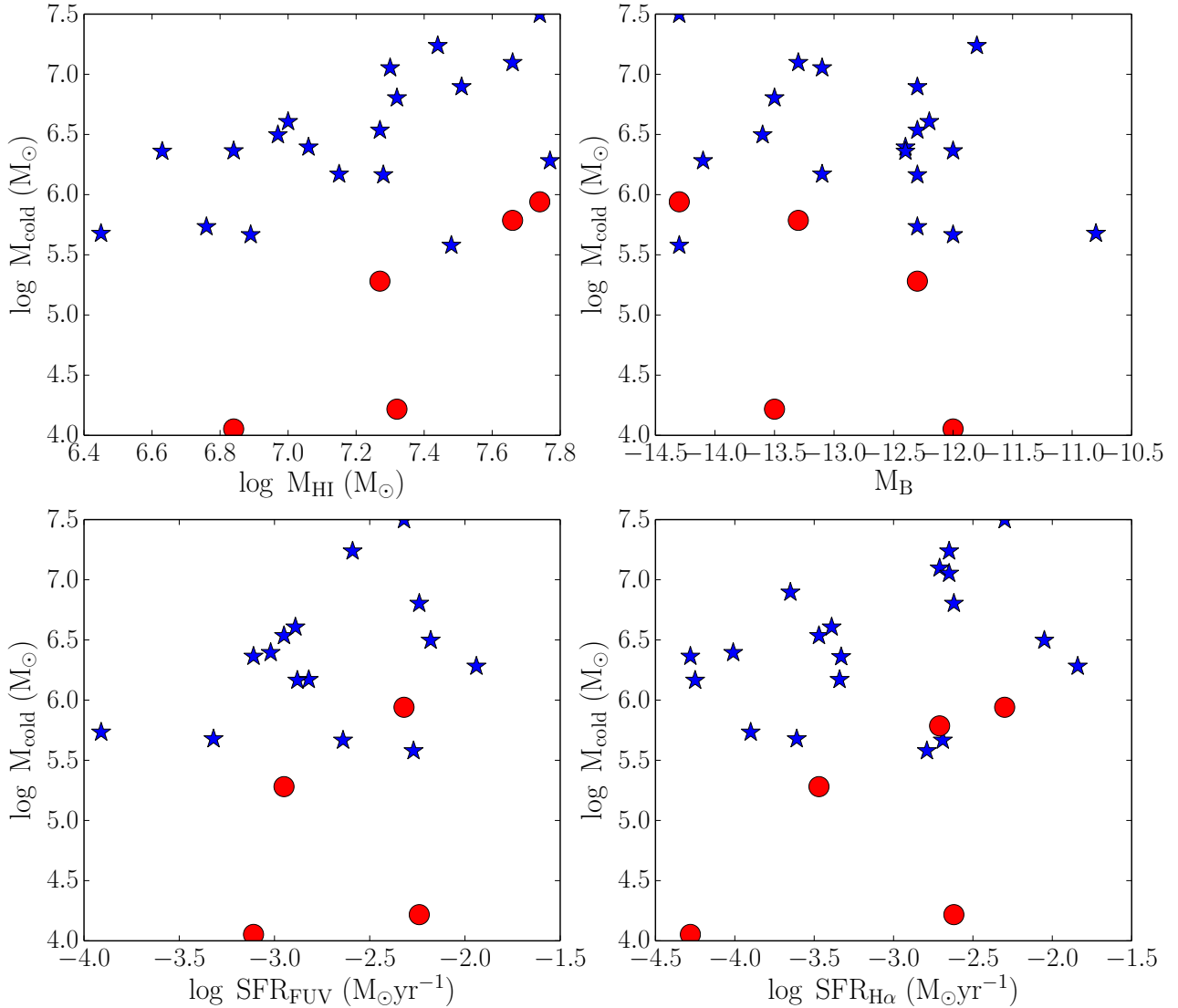


Figure 9. In all the panels, filled circles represents cold HI recovered by the Gaussian decomposition method while filled stars represents cold HI recovered by T_B method (optically thin approximation). Top left : The scatter plot of cold HI mass with total HI mass (M_{HI}). Top right : The scatter plot of cold HI mass with the absolute blue magnitude (M_B). Bottom left : The scatter plot of cold HI mass with star formation rate, as deduced from the FUV emission (SFR_{FUV}). Bottom right: The scatter plot of cold HI mass with star formation rate, as deduced from the $H\alpha$ star-formation rates ($SFR_{H\alpha}$). See the text for more details on the derivation of the star formation rates.

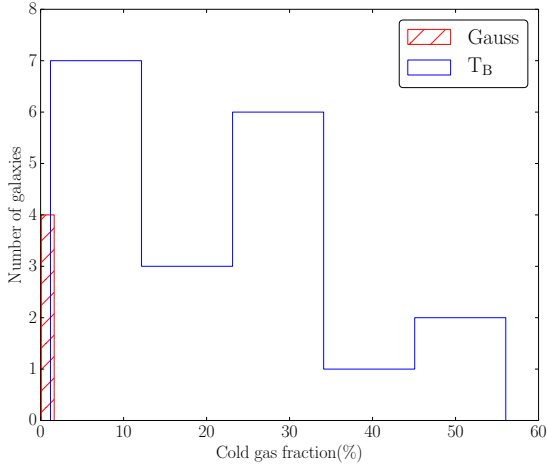
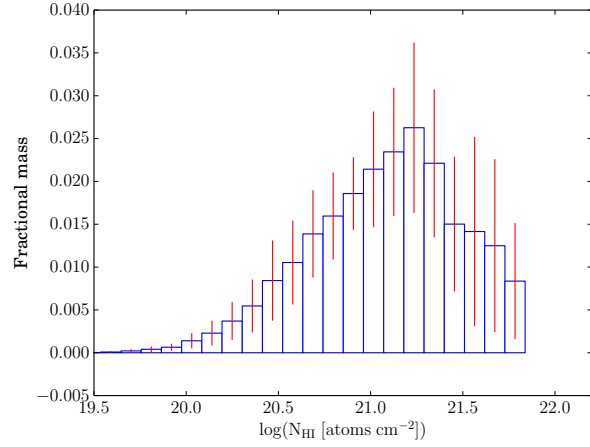
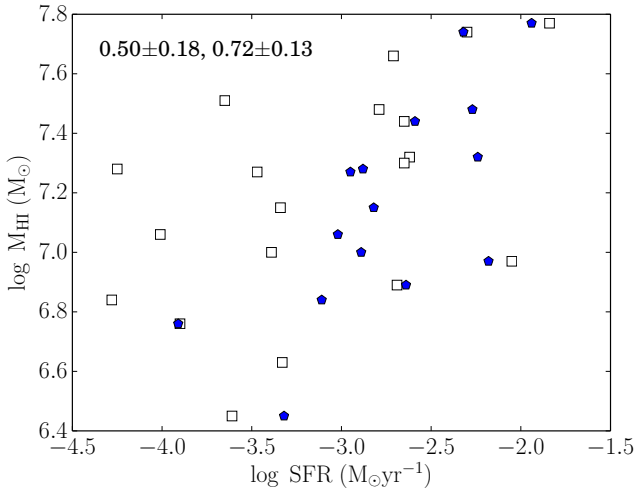
To investigate the connection between different global properties of galaxies and the detected cold HI, we plot the amount of cold HI as a function of different global parameters in Fig. 9. The global $H\alpha$ and FUV SFR used in the plots were taken from the Updated Nearby Galaxy Catalogue (UNGC) (Karachentsev, Makarov & Kaisina 2013). From the plots it is clear that brighter galaxies with more HI mass and higher star formation rates contain more cold HI. The correlation coefficients of the various parameters are listed in Tab. 5. The error bars have been estimated by bootstrap resampling. As can be seen from the table, the cold HI mass (as measured using the T_B method) does not appear to correlate with any of the other global parameters except the total HI mass and perhaps the FUV star formation rate. For cold gas measured using the Gaussian method, the number of galaxies in the sample are in general too small for any trends to be visible.

In Fig. 10, the total HI is plotted against total global star for-

mation rates. The numbers quoted on the top left of the figure represent the correlation coefficients for $H\alpha$, and FUV data respectively. Comparing with Fig. 9 one can see that the total HI correlates better with global star-formation than cold HI.

Conversion of atomic gas to the molecular phase is expected to lead to a maximum column density of the atomic phase. At column densities larger than this value the shielding against Lyman-Werner band photons which could dissociate the H_2 molecule (both self-shielding, as well as shielding due to dust) is expected to be insufficient so that the gas transitions from the atomic to the molecular phase. In our own galaxy for example, the molecular fraction becomes significant above column densities of $\log(N_{HI}) \sim 20.7$ (Savage et al. 1977; Gillmon & Shull 2006; Gillmon et al. 2006). If the gas to dust ratio scales with the metallicity one expects that the threshold column density would increase with decreasing metallicity (since lower metallicity would correspond to lower dust content

Method	M_{HI} vs M_{cold}	M_{B} vs M_{cold}	SFR_{FUV} vs M_{cold}	$\text{SFR}_{\text{H}\alpha}$ vs M_{cold}
Gauss	0.87 ± 0.22	-0.55 ± 0.44	0.29 ± 0.66	0.60 ± 0.43
T_{B}	0.57 ± 0.19	-0.26 ± 0.29	0.37 ± 0.22	0.32 ± 0.18

Table 5. Correlation between the cold HI mass and other global properties**Figure 8.** Histograms of cold gas fraction as detected by two different methods, i.e. Gaussian decomposition method and T_{B} method. As can be seen the T_{B} method detects much more cold gas as compared to Gaussian decomposition method.**Figure 11.** The fractional HI mass in the cold phase (as determined by the T_{B} method) as a function of N_{HI} . At $\log N_{\text{HI}} \sim 21.8$ cold HI fraction drops to zero, consistent with the expected threshold column density for conversion of low metallicity ($Z \sim 0.1 Z_{\odot}$) gas into the molecular phase. (Krumholz, McKee & Tumlinson 2009).**Figure 10.** Total HI mass is plotted against global star-formation rates. The empty squares represents $\text{H}\alpha$ data and blue pentagons represents FUV data. The numbers quoted on the top left shows the correlation coefficients between total HI and global star-formation rate for $\text{H}\alpha$ and FUV respectively.

and hence lower shielding). In Fig. 11 the fractional cold HI mass (i.e. the ratio of the cold HI mass detected over the entire sample to the total HI mass of the galaxies in the sample) is plotted as a function of the column density of the cold HI. As can be seen the fraction gradually increases with increasing N_{HI} but there is an abrupt cut off near $N_{\text{HI}} \sim 10^{21.8} \text{ atoms cm}^{-2}$. At low column

densities, one would expect that the gas would predominantly be in the WNM phase, and indeed in our own galaxy Kanekar, Braun & Roy (2011) show that there appears to be a threshold density of $\sim 10^{20.3} \text{ atoms cm}^{-2}$ for the formation of the CNM. Kanekar, Braun & Roy (2011) suggest that this threshold arises because one needs a critical amount of shielding before the gas can cool down to the CNM phase, while the numerical models of Kim, Ostriker & Kim (2014) indicates that this threshold can be understood in terms of vertical equilibrium in the local Milkyway disk. In our observations, since low N_{HI} would correspond to lower brightness temperature and hence a lower signal to noise ratio, the fall off that we see at low column densities could partly be a sensitivity related issue. What is more interesting is the peak HI column density of $\sim 10^{21.8}$ that is seen in our data. Krumholz, McKee & Tumlinson (2009) present detailed calculations of the atomic to molecular transition in gas of different metallicities. At the metallicity of our sample galaxies (i.e. $\sim 0.1 Z_{\odot}$), the saturation column density that is predicted by their model (Fig 1. in Krumholz, McKee & Tumlinson (2009)) is in excellent agreement with the maximum column density seen in Fig. 11.

5 CNM AND STAR FORMATION

5.1 The subsample and data preparation

In this section we investigate the correlation between CNM and star formation. We used GALEX FUV data and $\text{H}\alpha$ data mostly drawn from the Russian BTA telescope and the LVL survey (Dale et al. 2009) for estimating star formation rates. CNM was detected via the Gaussian decomposition method only in five galaxies and the

recovery efficiency is also very low. The cold HI detected using the Gaussian decomposition method is also spread over only a small number of independent beams. In contrast, from the T_B method, we detected cold HI in nineteen galaxies with significant number of independent beams per galaxy.

We used both $H\alpha$ and/or FUV data for estimating recent star formation for our sample galaxies. We detected cold HI using Gaussian decomposition method in 5 galaxies. Out of which, good quality $H\alpha$ data were available for two galaxies (UGC7605 and UGC0685). On the other hand good quality FUV data were available for all the galaxies except KKH11. For T_B method, our primary subsample consist of 19 galaxies for which cold HI was detected. Out of these 19 galaxies, good quality $H\alpha$ data were available for 9 galaxies. Three galaxies (ESO379-007, UGC8508 and KKH11) did not have GALEX observations and another four galaxies (KK200, KKH34, KKH6 and UGC5209) were observed as part of the all sky survey, and hence their FUV images have poor SNR. We exclude these seven galaxies from our sample which leaves us to a subsample of total 12 galaxies with good quality FUV GALEX data, as well as detected cold HI in T_B method.

In Table 6 we describe the general properties of this sample. The columns are as follows: Col. (1) Galaxy name, Col. (2) and (3) the equatorial coordinates (J2000), Col. (4) and (5) log of HI mass and absolute blue magnitude, Col. (6) inclination taken from (Karachentsev, Makarov & Kaisina 2013). They have been computed from the axial ratio of the optical disc, and the typical error is $\sim 10\%$. Col. (7) metallicity in solar unit, Col. (8) and (9) represents the global $H\alpha$ and FUV star-formation rates. Galaxies with detected cold HI in Gaussian decomposition and brightness temperature methods are marked with superscript ¹ and ² respectively. Galaxies with available $H\alpha$ data are marked with superscript ³ whereas ⁴ represents galaxies with available FUV star formation maps. The data in table 6 were taken from (Karachentsev, Makarov & Kaisina 2013).

5.1.1 Estimation of the star formation rate

FUV data were downloaded from the GALEX site and were used to prepare SFR_{FUV} maps for our sample galaxies. Only FUV (1350 – 1750Å) data were used to derive the star formation as a part of the NUV band (1750 – 2800Å) lies outside the range for which calibrations for conversion to the star formation rate are available. Emission from Galactic foreground stars was identified by manual inspection of the images, and removed from the FUV map using the task BLANK in AIPS. The foreground stars were identified and cross matched using the SDSS object identifier tool. The FUV maps were then smoothed to the resolution of the HI maps using the task SMOOTH in AIPS. The geometries of the smoothed FUV maps were then aligned with that of the HI maps using the task OHGEO. The FUV maps are in units of counts per second which can be converted into FUV flux using the calibration provided in GALEX site

$$m_{GALEX} = -2.5 \log(counts\ s^{-1}) \quad (1)$$

$$m_{AB} = m_{GALEX} + 18.82 \quad (2)$$

Using the above equations FUV flux maps were generated and corrected for the galactic dust extinction using the dust map of (Schlafly & Finkbeiner 2011). The formulae given by (Cardelli, Clayton & Mathis 1989) were used to extrapolate the extinction to the FUV band. For the internal dust correction, we adopt the approach described in Roychowdhury et al. (2014). Briefly, 25 μm

Spitzer observations of FIGGS galaxies were used to derive a numerical relation between the FUV star formation rate and the 24 μm flux. The 25 μm flux can be given as:

$$\log F_{25\mu m}(Jy) = 1.78 \log SFR_{FUV}(M_{\odot} yr^{-1}) + 2.62 \quad (3)$$

This corrected emergent FUV luminosity is then corrected for internal dust extinction using relation given by (Hao et al. 2011)

$$L_{FUV,corr} = L_{FUV,obs} + 3.89 L_{25\mu m} \quad (4)$$

The FUV luminosity of equation 4 can then be converted into the star formation rate using the calibration given by (Kennicutt & Evans 2012; Hao et al. 2011)

$$\log \dot{M}_*(M_{\odot} yr^{-1}) = \log L_x - \log C_x \quad (5)$$

where $L_x = \nu L_{\nu}$ is in the units of $ergs\ s^{-1}$ and $\log C_x = 43.35$. This calibration assumes an ongoing star formation for $\sim 10^8$ yr and a Salpeter IMF with solar metallicity. Studies of the star formation rate of nearby dIrr galaxies (Weisz et al. 2012) indicate that the assumption that the star formation rate has been approximately constant for the last $\sim 10^8$ yr is a reasonable one; however we do need to correct the star formation rate estimated above for the metallicity.

The typical metallicity of the dwarf galaxies in our sample is $Z \sim 0.1$ (Roychowdhury et al. 2014). Metallicity measurements are available only for a few of our sample galaxies (e.g. Marble et al. 2010; Moustakas & Kennicutt 2006). For the rest of our galaxies, we use the M_B -Z metallicity relation for dIrrs from (Ekta & Chengalur 2010) to estimate their metallicity. In Table 6 we list the metallicity estimated for our sample galaxies. The star formation rate estimated above hence needs to be corrected to account for this. Raiter, Schaerer & Fosbury (2010) calculate the emergent FUV fluxes in sub-solar metallicity environment using an evolutionary synthesis model assuming a continuous star formation for 10^8 yrs and a Salpeter IMF. They show that the emergent FUV flux increases by $\sim 11\%$, 19% , 27% & 32% for 0.4, 0.2, 0.05 and 0.02 times solar metallicity respectively. For each sample galaxy we do a linear interpolation between these tabulated values to get the metallicity correction to the FUV flux.

The star formation rate density was also computed using $H\alpha$ data largely taken from the 6m BTA telescope in Russia. For a detailed analysis of $H\alpha$ data see (Karachentsev & Kaisin 2007; Kaisin & Karachentsev 2008). The $H\alpha$ data were processed exactly the same way (foreground subtraction, smoothing to HI map resolution, geometrical alignment) as the FUV data. To derive the star-formation rate from $H\alpha$ map we used Kennicutt's calibration, equation (4) with L_x in the units of $ergs\ s^{-1}$ and $\log C_x = 41.27$. This calibration also assumes a Salpeter IMF with a continuous star-formation for 3 – 10 Myr. We note that at low star formation rates, the $H\alpha$ emission becomes unreliable as a tracer of the star formation rate largely because of stochasticity in the number of high mass stars observed at any instant (da Silva, Fumagalli & Krumholz 2014). The actual star formation rate as deduced from the $H\alpha$ emission for our sample should hence be treated with caution.

A detailed discussion of the error estimate for the star formation rates can be found in Roychowdhury et al. (2014), but for completeness we give a brief outline here. The total error in Σ_{SFR} is calculated as the quadrature sum of the individual errors. Firstly,

Table 6. Properties of the sub-sample galaxies selected for T_B method.

Name	RA (J2000)	DEC (J2000)	$\log M_{\text{HI}}$ (M_{\odot})	M_B	incl ($^{\circ}$)	Metallicity (Z_{\odot})	$\log \text{SFR}_{\text{H}\alpha}$ ($M_{\odot} \text{yr}^{-1}$)	$\log \text{SFR}_{\text{FUV}}$ ($M_{\odot} \text{yr}^{-1}$)
UGC00685 ^{1,2,3,4}	010722.3	+164102	7.74	-14.3	51	0.20 [†]	-2.30	-2.32
UGC06456 ^{2,3,4}	112800.6	+785929	7.77	-14.1	69	0.10 [‡]	-1.84	-1.94
UGC06541 ^{2,4}	113329.1	+491417	6.97	-13.6	65	0.13	-2.05	-2.18
UGC07298 ^{2,3,4}	121628.6	+521338	7.28	-12.3	67	0.06	-4.25	-2.88
DDO125 ^{2,3,4}	122741.8	+432938	7.48	-14.3	66	0.12	-2.79	-2.27
UGC07605 ^{1,2,3,4}	122839.0	+354305	7.32	-13.5	49	0.09	-2.62	-2.24
UGCA292 ^{2,3,4}	123840.0	+324600	7.44	-11.8	52	0.05	-2.54	-2.59
GR8 ^{2,4}	125840.4	+141303	6.89	-12.0	27	0.09	-2.69	-2.64
UGC08215 ^{1,2,4}	130803.6	+464941	7.27	-12.3	52	0.06	-3.47	-2.95
KK200 ^{1,4}	132436.0	-305820	6.84	-12.0	60	0.06	-4.28	-3.11
UGC08508 ^{2,3}	133044.4	+545436	7.30	-13.1	63	0.08	-2.65	—
UGC08833 ^{2,3,4}	135448.7	+355015	7.00	-12.2	30	0.06	-3.39	-2.89
DDO187 ^{2,4}	141556.5	+230319	7.06	-12.4	46	0.11 [†]	-4.01	-3.02
KKH98 ^{2,3,4}	234534.0	+384304	6.45	-10.8	67	0.04	-3.61	-3.32

^{1,2} Galaxies with detected cold HI in Gaussian decomposition and T_B method respectively

^{3,4} Galaxies with available $\text{H}\alpha$ and FUV map respectively

References - [†] : (Marble et al. 2010); [‡] : (Moustakas & Kennicutt 2006)

we adopt a 10% calibration error in FUV flux and a 15% calibration error in $\text{H}\alpha$ flux measurement. An additional error of $\sim 50\%$ in star formation rate is expected due the variation in IMF and star formation history (Leroy et al. 2012, 2013). Any other systematic errors are expected to be significantly smaller than the above errors. The total estimated error in the Σ_{SFR} for our sample galaxies is $\sim 50 - 55\%$.

5.1.2 Measurement of the cold HI column density

To compute the face on column density of cold gas and surface density of star formation rate at the same spatial location we deproject the observed column densities using the inclination angles given in Table 6. We also multiply the HI surface density by a factor 1.34 to account for the presence of helium. In several plots we average over several regions lying within a given Σ_{HI} , or Σ_{SFR} bin in order to improve the signal to noise ratio and reduce the effects of stochasticity in the star formation rate.

5.2 Results

5.2.1 Cold gas with associated star formation

To examine the association of cold HI with recent star formation, we compute the area covered by pixels with detected cold gas which also have a star formation rate density greater than the 3σ level of the SFR map, and normalizing this area by the total area covered by cold gas alone. In Fig. 12 we plot the histogram of fractional cold gas with associated star formation for our sample galaxies. The filled blue histogram present the fractional cold HI (detected in Gaussian decomposition method) associated with recent star formation as measured by the FUV emission. The filled magenta histogram represent the same but this time Σ_{SFR} is measured using $\text{H}\alpha$ map. The red empty step histogram represents fractional cold HI (as detected by T_B method) associated with recent star formation as traced by $\text{H}\alpha$, whereas hatched green histogram presents the fractional cold HI (detected in T_B method) associated with FUV star formation. From Fig. 12 it is implied that most of the cold HI (detected by either method) has some associated star

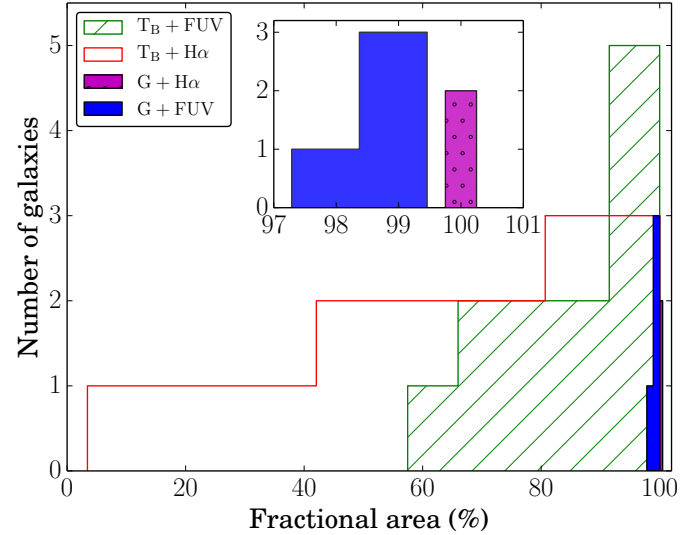


Figure 12. Histogram of areal fraction of cold HI with associated recent star formation. The filled magenta and blue histograms represents fractional cold HI detected in Gaussian decomposition method with associated star formation as traced by $\text{H}\alpha$ and FUV respectively. These histograms are zoomed in at the top middle portion of the figure for clarity. The red stepped and green hatched histograms represents fractional cold HI as detected in T_B method with associated recent star formation as traced by $\text{H}\alpha$ and FUV respectively. See text for discussion.

formation (as traced by either $\text{H}\alpha$ or FUV). We note that the number of galaxies having detected cold HI in Gaussian decomposition method and available $\text{H}\alpha$ and FUV maps are 2 and 4 respectively. The median fractional area of cold HI in T_B method with associated $\text{H}\alpha$ SFR is $\sim 71\%$ and with FUV SFR is $\sim 90\%$.

It is also interesting to ask the reverse question, i.e. if all star forming regions have associated cold HI or not. In Fig. 13, we show the fractional area with both cold HI and recent star formation normalised by total area covered by regions with recent star formation. The notations of the histograms are the same as in Fig. 12. As

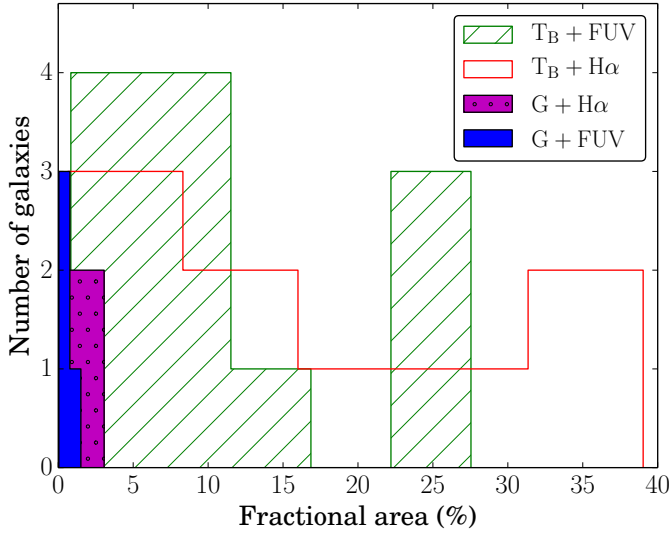


Figure 13. Histogram of areal fraction of recent star formation that is associated with cold H I. The notations are similar to that of Fig. 12. See text for more details.

the detection efficiency of Gaussian decomposition method is very poor, it is expected that most of the cold H I remains undetected and hence the fractional area of cold H I with associated recent star formation (both H α and FUV) found to be very less ($\lesssim 5\%$). But in T_B method, the fraction varies between few percent to 40% with a median value of $\sim 14\%$ for H α SFR and $\sim 8\%$ for FUV star formation. So, although most of the regions with cold H I have some associated recent star formation, the converse is not true. It is interesting to note that in the case of the recent star formation as estimated from the H α emission (which traces much more recent star formation than FUV) a larger fraction ($\sim 14\%$) of the star forming regions have associated cold H I. We show in Fig. 14 how this fraction varies as a function of the star formation rate. The red solid line represents FUV star formation whereas the black dashed line represents H α star formation. As can be seen, at the highest star formation rates, as traced by H α emission, almost all of the star forming regions ($\sim 80\%$) have associated cold gas. But at highest FUV star formation rates, $\sim 40 - 50\%$ star forming regions have associated star formation. As FUV traces an ongoing star formation for longer period of time, it is possible that star formation feedback destroys cold gas at highest FUV star forming sites. More sensitive data for larger number of galaxies is required for any firm conclusion.

5.2.2 The Kennicutt-Schmidt law for cold H I

In Fig. 15 we plot the star formation rate surface density as a function of cold gas surface density. In Gaussian decomposition method, cold H I is detected only in 5 galaxies with the gas distributed across only \sim a few independent beams per galaxy. Further only two of these galaxies have available H α maps and only four have available FUV maps. In total we have only 5-10 independent beams over which both the star formation rate and cold H I surface density measurements are available. Hence we exclude cold H I detected by Gaussian decomposition method for this study.

In Fig. 15 we show the H α as well as FUV star formation rate density of our sample galaxies as a function of cold gas sur-

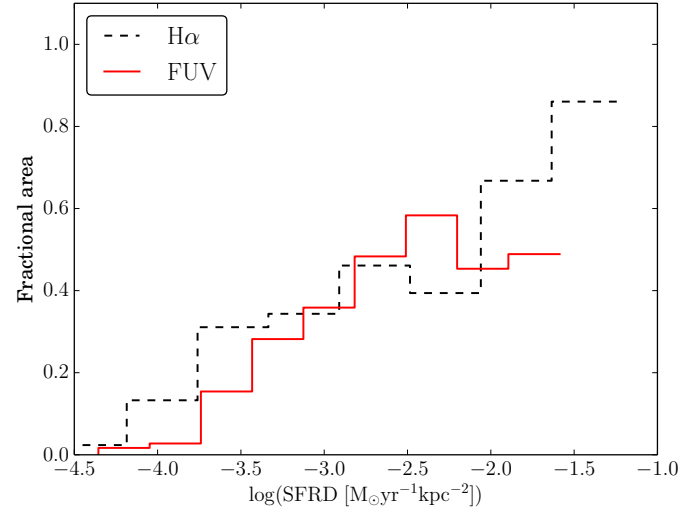


Figure 14. Histogram of areal fraction of recent star formation with associated cold H I, as a function of the star formation rate. The red solid histogram is for FUV SFR, whereas the black dotted histogram is for H α SFR. At the highest star formation rates as traced by H α (black dotted histogram), almost all of the star forming regions ($\sim 80\%$) have associated cold gas whereas $\sim 40 - 50\%$ star forming regions as traced by FUV (red solid histogram) have associated cold H I.

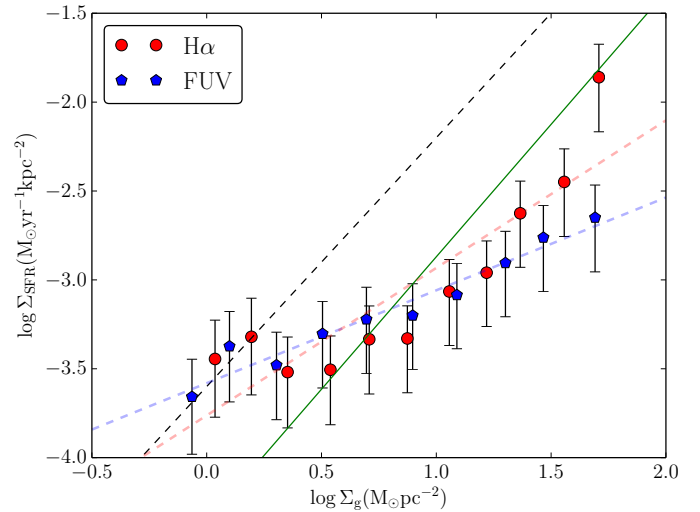


Figure 15. The Kennicutt-Schmidt law for cold H I. The red filled circles with error bars represent data points for our sample galaxies using the star formation rate as measured from the H α emission and the red thick dashed line is the straight line fit to these data points. The blue filled pentagons represent the data points for which star formation rate density is measured using FUV maps and the thick blue dashed line represents a straight line fit to these points. The green solid line represents K-S law for FIGGS galaxies (Roychowdhury et al. 2009), measured using the total gas content (i.e. not just the cold gas) at 400 pc resolution. The thin black dashed line represents the canonical K-S law (Kennicutt 1998).

face density (red circles and blue pentagons respectively). The error bars are the quadrature sum of the rms of the data in a given bin and the errors discussed in Sec. 5.1.1. The thick dashed red line represents a linear fit to the $H\alpha$ data. It has a slope of 0.83 ± 0.15 and an intercept of -3.76 ± 0.15 . The thick dashed blue line represents the fit to the FUV data. It has a slope of 0.52 ± 0.04 and an intercept of -3.58 ± 0.04 . The black dashed line represents the canonical K-S law (Kennicutt 1998) and the green solid line represents K-S law for FIGGS galaxies at 400 pc resolution (and using the total gas content, not just the cold gas) taken from (Roychowdhury et al. 2009). It can be seen that at the highest column densities the $H\alpha$ data points approach to the KS law determined using the total gas (green solid line). Further, although the Σ_{SFR} correlates with the cold gas column density, the slope is significantly flatter than that found using the total gas column density (e.g. Kennicutt 1997; Bigiel et al. 2008; Roychowdhury et al. 2009, 2014). This suggests that the total HI may be a better tracer of the star formation rate, (and the total molecular gas column density) than the cold HI alone. We note also that recent models of star formation in HI dominated region also find a flatter relationship between the Σ_{SFR} and the HI column density (Hu et al. 2015).

6 SUMMARY

We used two different methods to identify cold HI in a sample of dwarf irregular galaxies selected from the FIGGS and FIGGS2 survey. In the first method, line-of-sight HI spectra with SNR greater than 10 were decomposed into multiple Gaussian components. Following earlier studies, Gaussian components having velocity dispersion $\sigma < 6 \text{ km s}^{-1}$ were identified as cold HI. For a galaxy that is in common between the two samples, we compare narrow velocity dispersion HI detected using this method with that detected using the same technique (but with a different data set, and a different software routine) by (Warren et al. 2012). In our sample we detect narrow velocity dispersion components in 5 galaxies out of the total sample of 12. In common with previous studies, we find that the narrow velocity dispersion components do not overlap with the locations of the highest column density HI or the locations of the brightest $H\alpha$ emission. This is somewhat surprising if the narrow velocity dispersions are accurately tracing the cold gas content of the galaxies.

We hence used a different method to try and identify cold atomic gas. Since the WNM has low opacity, there is a limit to the brightness temperature expected from physically plausible path lengths through the WNM. Gas with higher T_B than this threshold must be associated with cold gas. Since the CNM is clumpy, high velocity and spatial resolution is required to identify the high T_B gas. We re-imaged our sample galaxies at 100 pc and identified all regions with $T_B > 50 \text{ K}$ as being associated with the CNM. We find that cold gas identified in this way is associated with regions of high HI column density as well as regions with on going star formation. The amount of gas identified as being cold by the T_B method is also significantly larger than the amount of gas identified as being cold using Gaussian Decomposition. We compare the peak HI column density that we observe (at 100 pc resolution) with the largest column density expected in low metallicity gas, and find good agreement with theoretical models.

We study the relationship between the cold HI detected using the T_B method and recent star formation. For our sample of galaxies we find that regions with cold HI are almost always have associated recent star formation. $\sim 70\%$ of the cold gas has some asso-

ciated recent star formation as traced by $H\alpha$ emission and $\sim 90\%$ of the cold gas are associated with star formation as measured by FUV emission. The converse however is not true, only $\sim 10-15\%$ of the area covered by regions with recent star formation is associated with cold HI. In the case of $H\alpha$ emission (which traces more recent star formation) the fraction of star forming regions that are associated with cold HI is significantly higher. In fact, at the highest star formation rates, almost all of the star forming regions are associated with cold HI. If we focus on the regions where there is overlap between cold gas and recent star formation, we find that Σ_{SFR} correlates to Σ_{HI} , albeit with a slope ($\sim 0.83 \pm 0.15$ for $H\alpha$ and 0.52 ± 0.04 for FUV star formation) that is significantly flatter than that seen in earlier studies which used the total (as opposed to the cold) gas content.

7 APPENDIX

REFERENCES

- Audit E., Hennebelle P., 2005, *A&A*, 433, 1
 Baker P. L., Burton W. B., 1975, *ApJ*, 198, 281
 Begum A., Chengalur J. N., Bhardwaj S., 2006, *MNRAS*, 372, L33
 Begum A., Chengalur J. N., Karachentsev I. D., Sharina M. E., Kaisin S. S., 2008, *MNRAS*, 386, 1667
 Bigiel F., Leroy A., Walter F., Brinks E., de Blok W. J. G., Madore B., Thornley M. D., 2008, *AJ*, 136, 2846
 Braun R., 1997, *ApJ*, 484, 637
 Braun R., 2012, *ApJ*, 749, 87
 Braun R., Walterbos R. A. M., 1992, *ApJ*, 386, 120
 Cannon J. M. et al., 2011, *ApJL*, 739, L22
 Cardelli J. A., Clayton G. C., Mathis J. S., 1989, *ApJ*, 345, 245
 Chengalur J. N., Kanekar N., Roy N., 2013, *MNRAS*, 432, 3074
 Clark B. G., 1965, *ApJ*, 142, 1398
 da Silva R. L., Fumagalli M., Krumholz M. R., 2014, *MNRAS*, 444, 3275
 Dale D. A. et al., 2009, *ApJ*, 703, 517
 de Blok W. J. G., Walter F., 2006, *AJ*, 131, 363
 Ekta B., Chengalur J. N., 2010, *MNRAS*, 406, 1238
 Field G. B., Goldsmith D. W., Habing H. J., 1969, *ApJL*, 155, L149
 Field G. B., Saslaw W. C., 1965, *ApJ*, 142, 568
 Gillmon K., Shull J. M., 2006, *ApJ*, 636, 908
 Gillmon K., Shull J. M., Tumlinson J., Danforth C., 2006, *ApJ*, 636, 891
 Hao C.-N., Kennicutt R. C., Johnson B. D., Calzetti D., Dale D. A., Moustakas J., 2011, *ApJ*, 741, 124
 Heiles C., Troland T. H., 2003a, *ApJS*, 145, 329
 Heiles C., Troland T. H., 2003b, *ApJS*, 145, 329
 Heiles C., Troland T. H., 2003c, *ApJ*, 586, 1067
 Hu C.-Y., Naab T., Walch S., Glover S. C. O., Clark P. C., 2015, *ArXiv e-prints*
 Hunter D. A. et al., 2012, *AJ*, 144, 134
 Kaisin S. S., Karachentsev I. D., 2008, *A&A*, 479, 603
 Kanekar N., Braun R., Roy N., 2011, *ApJL*, 737, L33
 Kanekar N., Chengalur J. N., 2003, *A&A*, 399, 857
 Kanekar N., Chengalur J. N., de Bruyn A. G., Narasimha D., 2003, *MNRAS*, 345, L7
 Karachentsev I. D., Kaisin S. S., 2007, *AJ*, 133, 1883
 Karachentsev I. D., Makarov D. I., Kaisina E. I., 2013, *AJ*, 145, 101

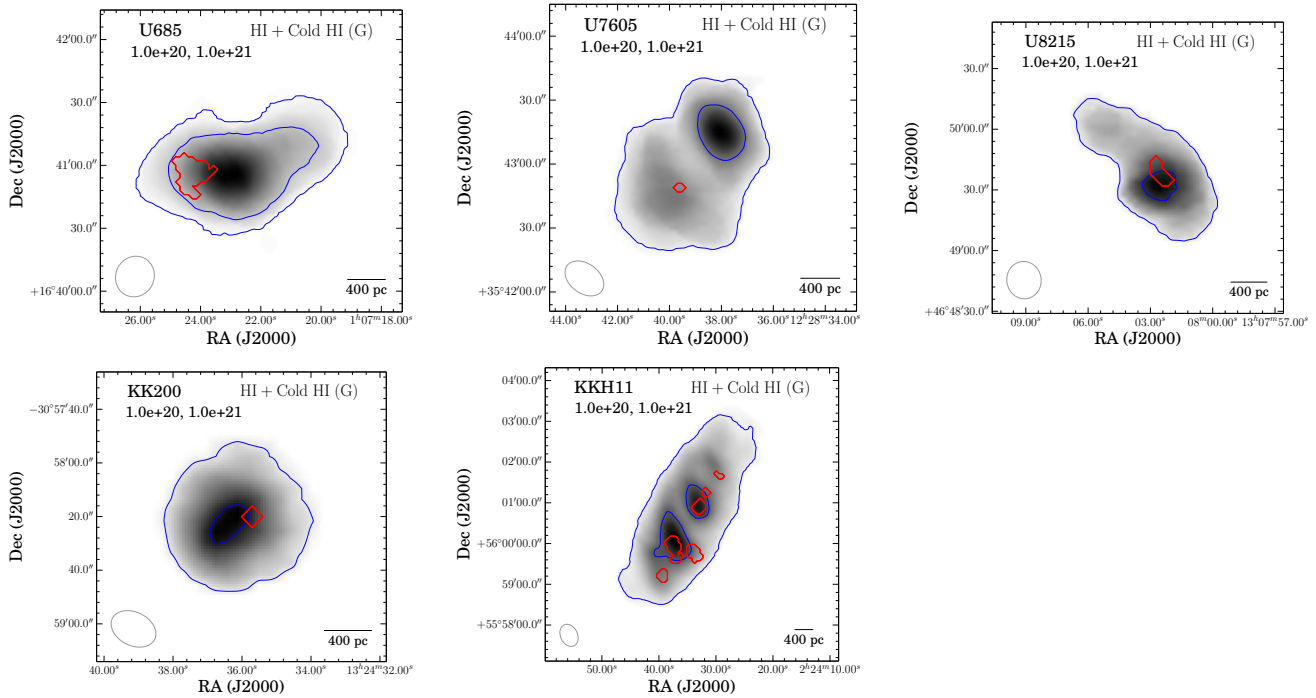


Figure 16. Overlays of HI (at 400 pc resolution, contours) with cold HI as detected by Gaussian decomposition method. The total HI is in gray scale with two blue contours representing two characteristic column densities as quoted on the top left corner. The red contour represents location of detected cold HI in Gaussian decomposition method. As the cold HI was not detected over many beams, the red contours are mostly representing same column density region.

Kennicutt R. C., 1997, in *Astrophysics and Space Science Library*, Vol. 161, *Astrophysics and Space Science Library*, pp. 171–195
 Kennicutt R. C., Evans N. J., 2012, *ARA&A*, 50, 531
 Kennicutt, Jr. R. C., 1998, *ApJ*, 498, 541
 Kim C.-G., Ostriker E. C., Kim W.-T., 2014, *ApJ*, 786, 64
 Krumholz M. R., McKee C. F., Tumlinson J., 2009, *ApJ*, 699, 850
 Leroy A. K. et al., 2012, *AJ*, 144, 3
 Leroy A. K. et al., 2013, *ApJL*, 769, L12
 Marble A. R. et al., 2010, *ApJ*, 715, 506
 Moustakas J., Kennicutt, Jr. R. C., 2006, *ApJS*, 164, 81
 Ott J. et al., 2012, *AJ*, 144, 123
 Radhakrishnan V., Goss W. M., 1972, *ApJS*, 24, 161
 Raiter A., Schaerer D., Fosbury R. A. E., 2010, *A&A*, 523, A64
 Rohlfs K., 1971, *A&A*, 12, 43
 Roy N., Kanekar N., Braun R., Chengalur J. N., 2013, *MNRAS*, 436, 2352
 Roy N., Kanekar N., Chengalur J. N., 2013a, *MNRAS*, 436, 2366
 Roy N., Kanekar N., Chengalur J. N., 2013b, *MNRAS*, 436, 2366
 Roychowdhury S., Chengalur J. N., Begum A., Karachentsev I. D., 2009, *MNRAS*, 397, 1435
 Roychowdhury S., Chengalur J. N., Kaisin S. S., Karachentsev I. D., 2014, *MNRAS*, 445, 1392
 Savage B. D., Bohlin R. C., Drake J. F., Budich W., 1977, *ApJ*, 216, 291
 Schlafly E. F., Finkbeiner D. P., 2011, *ApJ*, 737, 103
 Schmidt M., 1957, *BAN*, 13, 247
 Shuter W. L. H., Verschuur G. L., 1964, *MNRAS*, 127, 387
 Swarup G., Ananthakrishnan S., Kapahi V. K., Rao A. P., Subrahmanya C. R., Kulkarni V. K., 1991, *Current Science*, Vol. 60, NO.2/JAN25, P. 95, 1991, 60, 95
 Warren S. R. et al., 2012, *ApJ*, 757, 84
 Weisz D. R. et al., 2012, *ApJ*, 744, 44

Wolfire M. G., Hollenbach D., McKee C. F., Tielens A. G. G. M., Bakes E. L. O., 1995a, *ApJ*, 443, 152
 Wolfire M. G., McKee C. F., Hollenbach D., Tielens A. G. G. M., 1995b, *ApJ*, 453, 673
 Wolfire M. G., McKee C. F., Hollenbach D., Tielens A. G. G. M., 2003, *ApJ*, 587, 278
 Young L. M., Lo K. Y., 1996, *ApJ*, 462, 203
 Young L. M., Lo K. Y., 1997, *ApJ*, 490, 710
 Young L. M., van Zee L., Lo K. Y., Dohm-Palmer R. C., Beierle M. E., 2003, *ApJ*, 592, 111

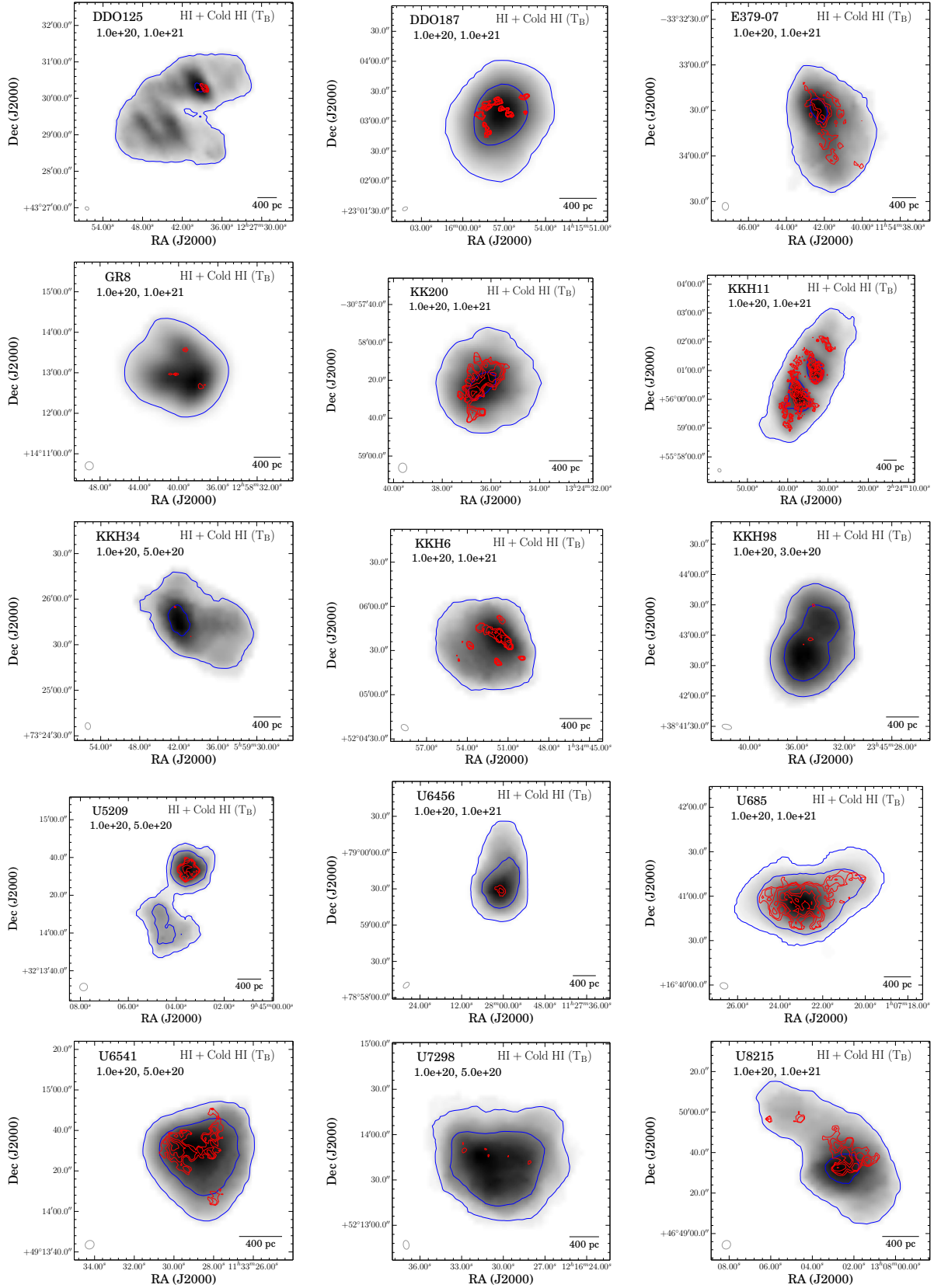


Figure 17. Overlays of cold HI detected using the T_B method (red contours) on the total HI as traced by 400pc resolution HI MOMNT maps (gray scale). The beam at the bottom left corner represents the resolution of the cold HI recovered in T_B method. The conventions for the blue contours are the same as in Fig. 16.

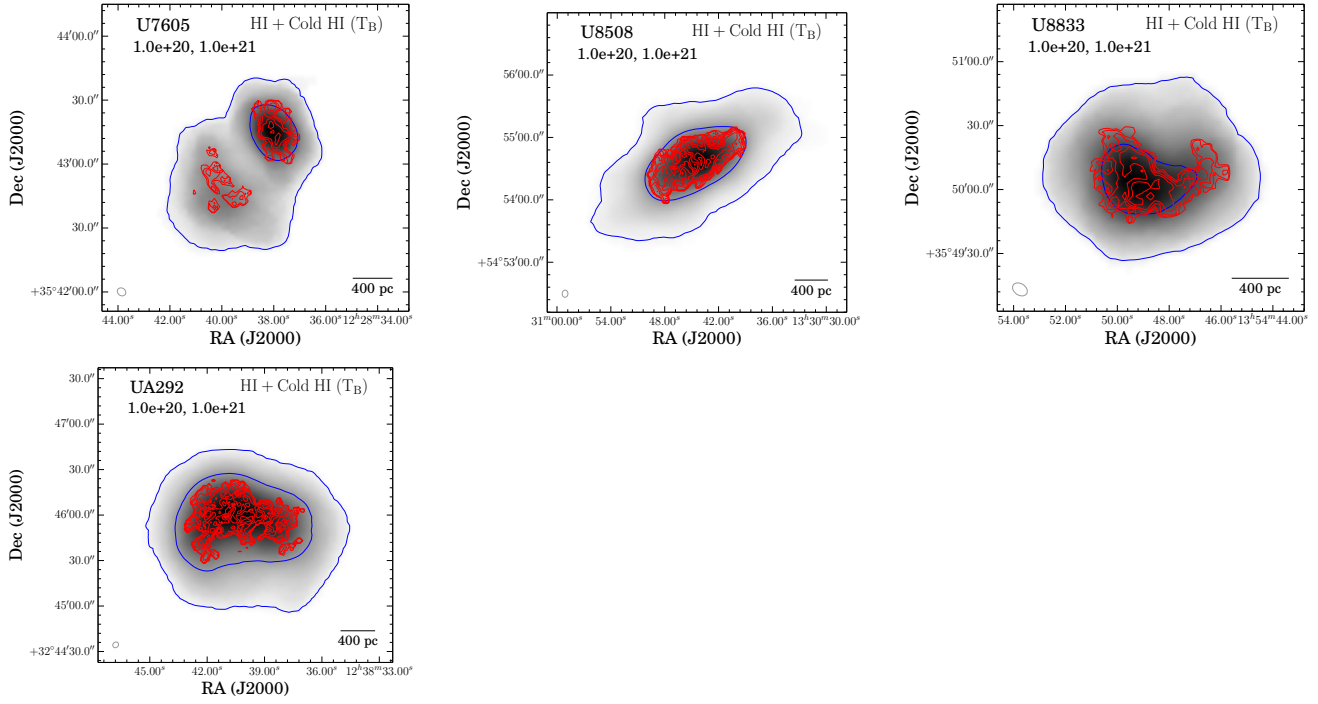


Figure 18. Continuation of Fig. 17

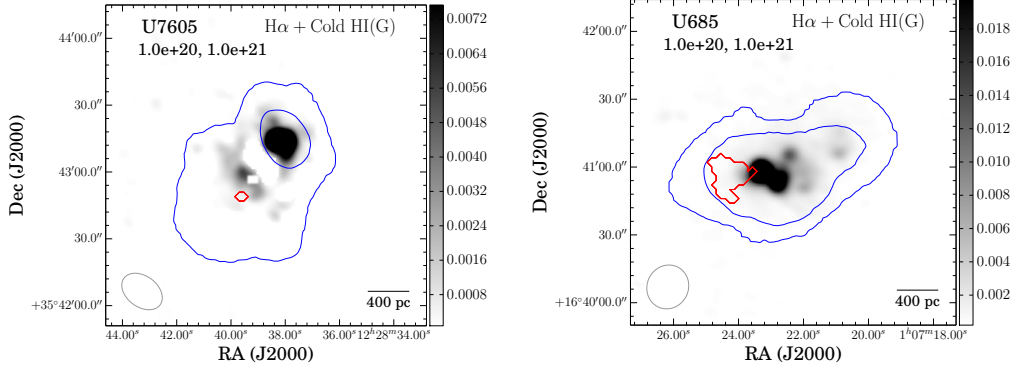


Figure 19. Overlays of cold HI detected using the Gaussian decomposition method (red contours) on H α star formation in gray scale. The blue contours are the same as Fig. 16. The colorbar represents the H α star formation rate density in the unit of $M_{\odot} \text{yr}^{-1} \text{kpc}^{-2}$.

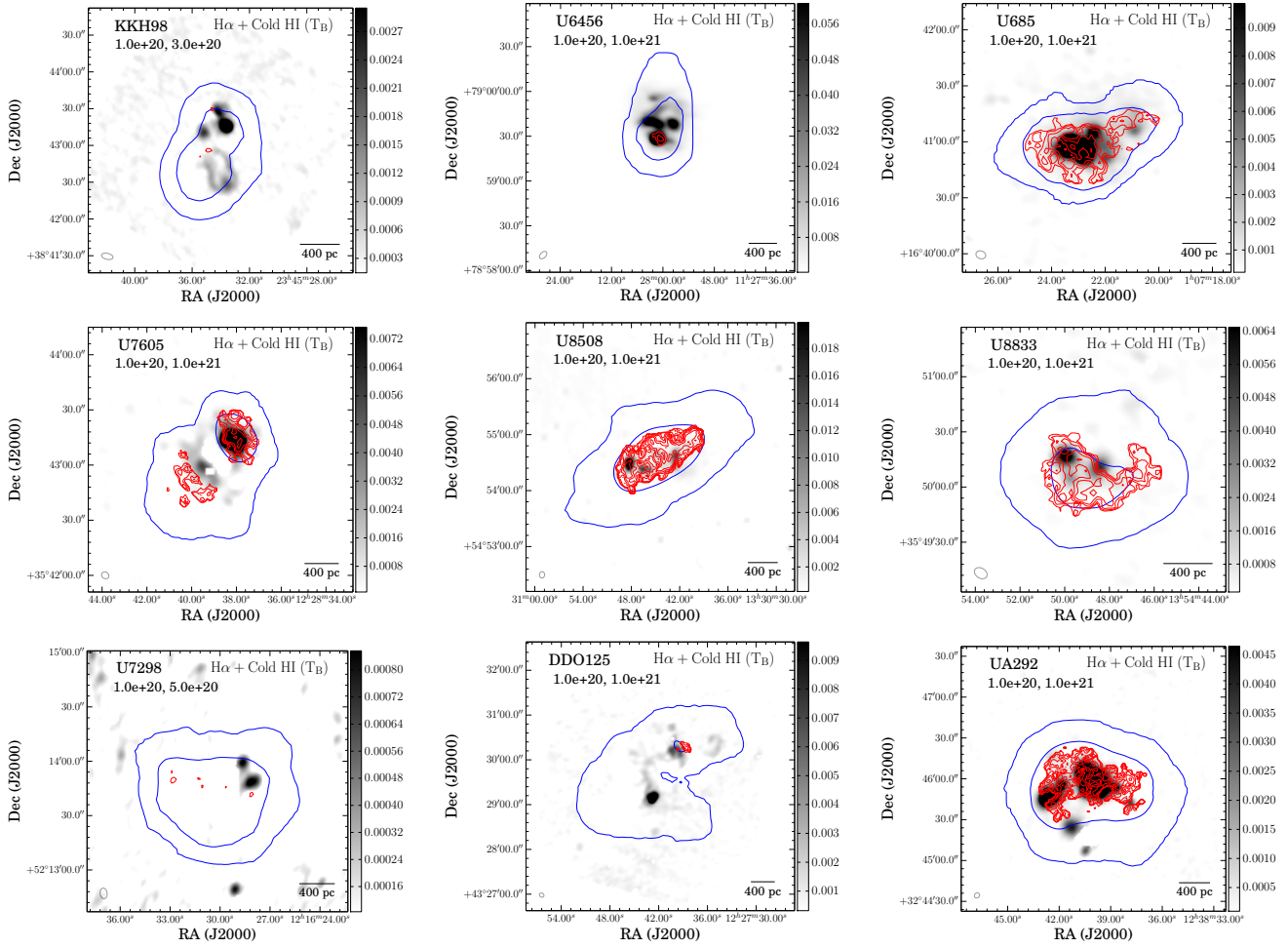


Figure 20. Overlays of cold HI detected using the T_B method (red contours) on $H\alpha$ star formation rate density (gray scale). Color bars are in the units of $M_{\odot} \text{yr}^{-1} \text{kpc}^{-2}$. The blue contours are the same as in Fig. 16. The beam at the bottom left corner of every panel represents the resolution of the cold HI map.

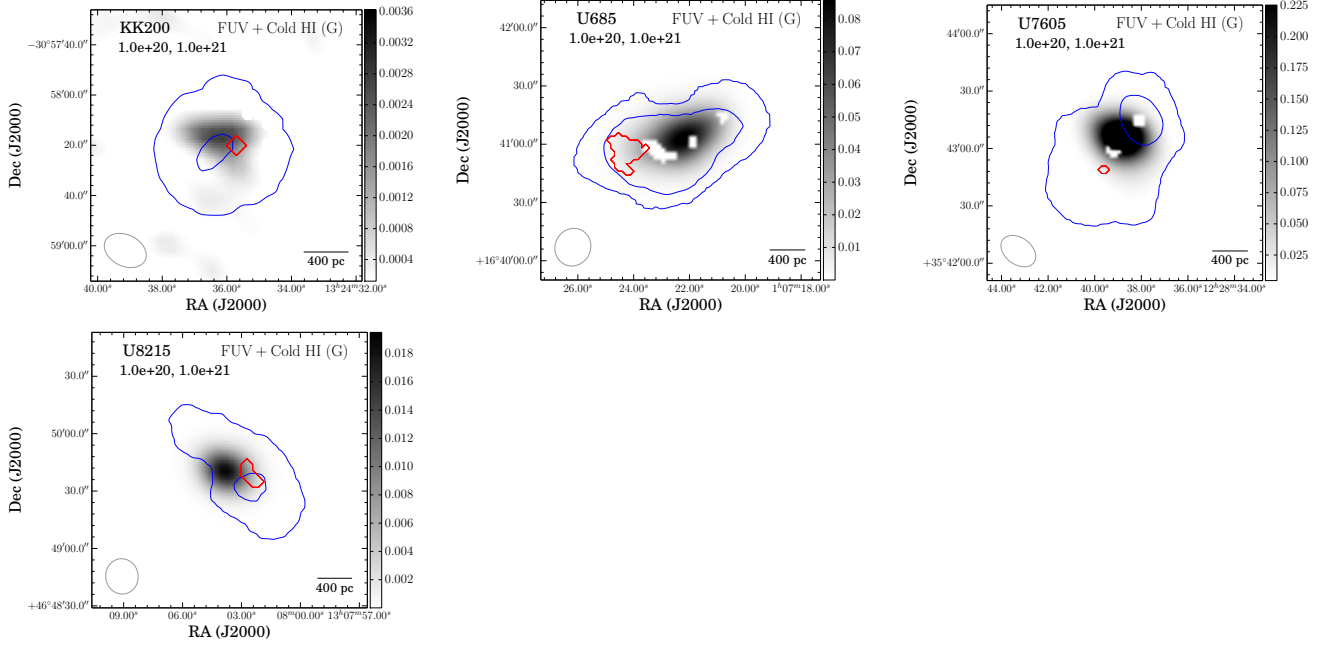


Figure 21. Overlays of cold HI detected using the Gaussian decomposition method (red contours) on FUV star formation rate density (gray scale). Color bars are in the units of $M_{\odot} \text{yr}^{-1} \text{kpc}^{-2}$. The blue contours are the same as in Fig. 16.

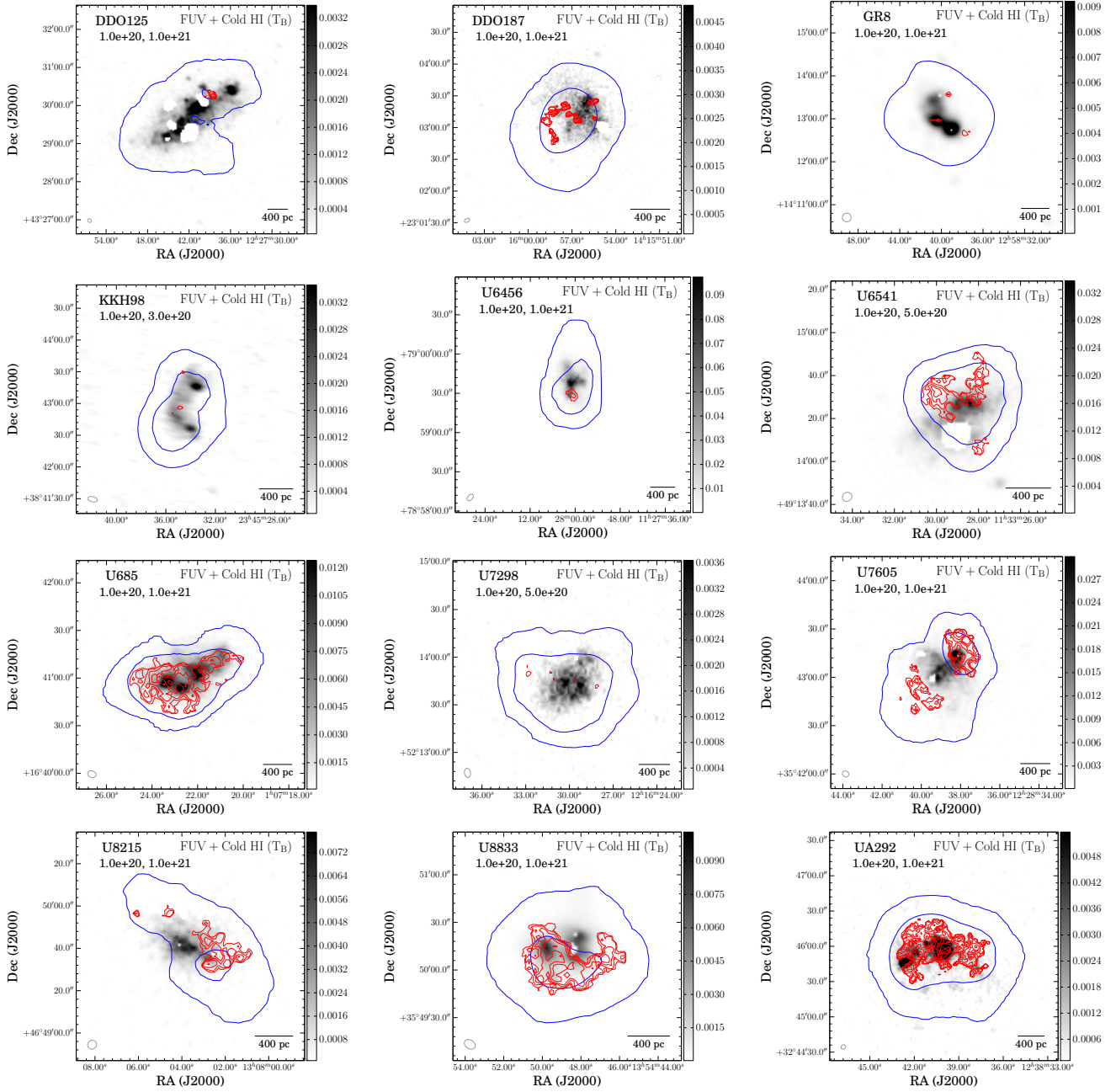


Figure 22. Overlays of cold HI detected using the T_B method (red contours) on FUV star formation rate density (gray scale). Color bars are in the units of $M_{\odot} \text{yr}^{-1} \text{kpc}^{-2}$. The blue and red contours are the same as in Fig. 20. The beam at the bottom left corner of every panel represents the resolution of the cold HI map.